Pneumococcal H_2O_2 Reshapes Mitochondrial Function and Reprograms Host Cell Metabolism

Anna Scasny[1], Babek Alibayov[1], Ngoc Hoang[2], Ana G. Jop Vidal[1], Kenichi Takeshita[1], Consuelo Bautista[1], Eva Bengten[1,3], Antonino Baez[1,4], Wei Li[5], Jonathan Hosler[1], Kurt Warncke[5], Kristin Edwards[2], Jorge E. Vidal[1,3]

[1]Department of Cell and Molecular Biology, [2]Department of Pharmacology and Toxicology, [3]Center for Immunology and Microbial Research, School of Medicine, University of Mississippi Medical Center, Jackson, MS; [4]Centro de Investigaciones en Ciencias Microbiológicas (CICM), Instituto de Ciencias (IC), Benemérita Universidad Autónoma de Puebla (BUAP), Puebla, México; [5]Department of Physics, Emory University, Atlanta GA

Running title: Spn-H_2O_2 drives metabolic reprograming

#Address correspondence to:
Jorge E. Vidal, PhD
2500 North State Street, Jackson Mississippi 39216
Phone: (601) 984-1711, Fax: (601) 984-1708
Email jvidal@umc.edu,

Abstract

Streptococcus pneumoniae (Spn), a primary cause of pneumonia, induces acute lung parenchymal damage through a unique metabolic pathway generating hydrogen peroxide (H_2O_2) as a byproduct. This study demonstrates that Spn-derived H_2O_2, primarily produced by pyruvate oxidase (SpxB), inhibits key tricarboxylic acid (TCA) cycle enzymes (aconitase, glutamate dehydrogenase, and α-ketoglutarate dehydrogenase) in lung epithelial cells, leading to citrate accumulation and diminished NADH production for oxidative phosphorylation. RNA sequencing reveals SpxB-dependent upregulation of glycolytic genes (HIF1A, IER3, HK2, PFKP), restricting pyruvate entry into the TCA cycle and increasing glucose consumption and lactate/acetate production, indicative of a Warburg-like metabolic shift that may enhance bacterial survival. Notably, mitochondrial membrane potential remains largely preserved, with minimal apoptosis despite Spn-induced stress. These findings uncover a novel mechanism of Spn-driven host metabolic reprogramming, highlighting potential therapeutic targets for pneumococcal diseases.

Importance

Streptococcus pneumoniae remains a leading cause of community-acquired pneumonia worldwide, yet the mechanisms by which it manipulates host metabolism to promote its survival and pathogenesis are not fully understood. This study reveals a novel metabolic strategy whereby pneumococcus-derived hydrogen peroxide, generated by pyruvate oxidase (SpxB), disrupts the host TCA cycle and drives a Warburg-like metabolic shift in lung epithelial cells. By inhibiting key TCA cycle enzymes and rewiring glycolytic gene expression, S. pneumoniae effectively reprograms host cell metabolism to favor its persistence, while minimizing host cell apoptosis and maintaining mitochondrial function. These insights expand our understanding of host-pathogen metabolic interactions and identify potential metabolic vulnerabilities that could be targeted to mitigate tissue damage and improve treatment outcomes in pneumococcal pneumonia.

Introduction.

Streptococcus pneumoniae (Spn), commonly known as the pneumococcus, is a major global health burden, particularly among children and the elderly, causing significant morbidity and mortality through pneumonia and other invasive pneumococcal diseases (IPDs)(1, 2). During pneumococcal pneumonia, lung colonization induces profound cellular damage, disrupting critical structural components such as ciliary function, β-actin architecture, and nuclear and mitochondrial DNA (3-5). Despite progress in understanding pneumococcal pathogenesis, the mechanisms driving host cell death and tissue injury remain incompletely elucidated.

A hallmark of Spn pathogenesis is its efficient metabolic activity, primarily driven by glycolysis, which supports energy and biomass production through glucose catabolism. A critical byproduct, hydrogen peroxide (H_2O_2), a reactive oxygen species, is increasingly implicated in host cell damage (1, 6). Spn produces H_2O_2 continuously via glycolysis, its primary ATP-generating pathway, with some strains generating up to 2 mM H_2O_2, which is detectable both extracellularly and intracellularly(7-9). Pyruvate oxidase (SpxB) and lactate oxidase (LctO) primarily drive H_2O_2 production, with SpxB converting pyruvate to acetyl phosphate and LctO oxidizing lactate to pyruvate, both yielding H_2O_2 (9, 10). SpxB accounts for ~85% of total H_2O_2 production in Spn, while LctO contributes ~15%, reflecting adaptations to oxygen-rich environments like the lungs (9, 10).

Substantial evidence implicates Spn-derived H_2O_2 (hereafter Spn-H_2O_2) in host cell death and disease severity in animal models (11-16). Our previous studies have shown that Spn-H_2O_2 inhibits *ex vivo* Complex I-driven respiration (CIDR)(17). Additionally, Spn infection induces mitochondrial DNA leakage in lung cells, triggering a type I interferon response (18),

and in an aged murine model of pneumonia, it dysregulates mitochondrial complex expression, elevates oxidative stress, and impairs antioxidant defenses, leading to reduced ATP production (19). These findings underscore the role of H_2O_2 in disrupting mitochondrial function, exacerbating cytotoxicity. Furthermore, Spn alters host cell nutrient availability by depleting epithelial glycans and enhancing macrophage glutamine uptake, thereby increasing bacterial access to host-derived carbohydrates and amino acids during infection (20). These metabolic shifts fuel bacterial proliferation and inflammation, driving disease progression. Concurrently, Spn infection activates both apoptosis and pyroptosis, indicating complex cytotoxic mechanisms (3, 4, 21, 22). Our recent studies reveal that Spn-H_2O_2 disrupts actin and tubulin cytoskeletons in bronchial and alveolar epithelial cells, impairing structural stability and protein trafficking, leading to microtubule catastrophe and cell swelling due to loss of actin stress fibers (17, 23). This mirrors cytoskeletal damage in ventricular cardiomyocytes exposed to 100 μM H_2O_2, where oxidation of specific cysteine residues (Cys213, Cys295, and Cys305 in α-globin; Cys129 in β-globin) disrupts tubulin interactions, inhibiting microtubule polymerization (24-26). Moreover, Spn-H_2O_2 oxidizes hemoglobin *in vitro* and *in vivo*, inducing aggregation via crosslinking of α- and β-globin chains (27, 28) and generating MetOH, a product of methionine-55 oxidation in the β-chain linked to globin collapse (23).

Mitochondria are essential for many cellular functions, with two main functions being to produce ATP through oxidative phosphorylation (OXPHOS) and regulate programmed cell death (29). The tricarboxylic acid (TCA), or Krebs, cycle, a central metabolic pathway, supplies essential intermediates such as NADH to the electron transport chain (ETC) for ATP synthesis (30). In this process, exergonic electron transfer to O_2 is coupled to the endergonic phosphorylation of ADP to ATP via four ETC complexes (I–IV), which contain heme- or iron-

sulfur (Fe-S)-containing proteins (31, 32). For instance, complexes I and III include Fe-S proteins, while complexes II, III, and IV incorporate hemoproteins with hemes b, c, and a, respectively; soluble cytochrome c (Cyt*c*) also carries heme c (31, 33). We have previously demonstrated that Spn-H_2O_2 oxidizes soluble Cyt*c* *(17, 34)*, and this oxidant is produced intracellularly during pneumococcal invasion of lung cells (23), highlighting a direct mechanism of mitochondrial disruption.

To establish infection, Spn invades bronchial and alveolar epithelial cells, adapting to the intracellular environment for survival and proliferation. Spn's metabolic configuration resembles that of mitochondria under stress conditions (e.g., hypoxia), with an incomplete TCA cycle lacking α-ketoglutarate dehydrogenase, which converts α-ketoglutarate to succinyl-CoA, forcing reliance on glycolysis for energy production in resource-limited niches (35, 36). Similarly, Spn possesses a partial electron transport chain (ETC), missing NADH:quinone oxidoreductase (complex I-like) and cytochrome bc1 complex (complex III-like), but encoding a minimal succinate dehydrogenase (complex II-like) for fumarate reduction, a cytochrome bd oxidase (complex IV-like) for oxygen reduction, and an ATP synthase (complex V-like) likely for proton homeostasis. This configuration, while suited for oxygen-limited environments, mirrors mitochondrial ETC reliance on cytochrome oxidases but results in continuous H_2O_2 production, amplifying oxidative stress in host cells. The absence of a robust TCA cycle and ETC also impairs Spn's ability to detoxify reactive oxygen species, exacerbating host cell damage. Furthermore, Spn exploits host resources by scavenging metabolites such as amino acids and carbohydrates, upregulating glutamine uptake and depleting epithelial glycans to fuel its metabolism and enhance virulence (20). These metabolic adaptations highlight Spn's ability to disrupt host cellular processes through strategic reprogramming, motivating this study to

investigate the H_2O_2-mediated effects on host mitochondrial function and metabolism during pneumococcal infection.

RESULTS

Oxidation of Cyt*c* by *S. pneumoniae*-H_2O_2 creates a tyrosyl radical. Spn-H_2O_2 is known to oxidize heme groups in hemoglobin and Cyt*c,* key components of the mitochondrial ETC (17, 23, 34). To investigate the kinetics of H_2O_2-mediated Cyt*c* oxidation, Todd-Hewitt broth supplemented with yeast extract (THY) was enriched with 56 µM Cyt*c* (THY-Cyt*c*) and inoculated with Spn. Supernatants from time-course experiments were analyzed by spectroscopic methods to assess oxidation dynamics (37, 38). Compared to mock-inoculated THY-Cyt*c* cultures, statistically significant heme degradation was observed in those incubated with TIGR4 for 6 h (Fig. 1A) and in those inoculated with EF3030 and incubated for 4 and 6 h (Fig. 1C). In mock-inoculated THY-Cyt*c* cultures incubated for up to 6 h, the Soret peak of heme-Fe^{3+} exhibited a maximum absorbance at 405 nm (Fig. 1B and 1D). In contrast, heme degradation observed in cultures of Spn strains, TIGR4 (Fig. 1B) or EF3030 (Fig. 1D) was characterized by the significant loss of the Soret peak and the appearance of a different species absorbing at 325 nm (Fig. 1B and 1D, arrow). Heme degradation and the formation of the 305 nm species were not detected in cultures of wt strains treated with catalase or in cultures of strains deficient in Spn-H_2O_2 production such as TIGR4Δ*spxB*Δ*lctO* or EF3030Δ*spxB*Δ*lctO* (Fig. 1B and 1D).

The α and β absorption peaks of Cyt*c*, observed at 550 and 520 nm, respectively (39, 40) underwent oxidation in 6 h cultures of TIGR4 (Fig. 1E) and EF3030 (Fig. 1F) indicative of porphyrin ring degradation. Notably, TIGR4Δ*spxB*Δ*lctO* retained residual oxidative activity on the α and β peaks, possibly via minor SpxB/LctO-independent pathways. This residual activity

was completely abrogated upon catalase treatment (Fig. 1E), underscoring the role of H_2O_2 in driving heme degradation in these strains.

Previous studies have shown that H_2O_2 oxidation of hemoproteins generates highly reactive and toxic radicals, including the ferryl radical ($^{\bullet}Hb^{4+}$), and tyrosyl radical (5, 41-44). To determine whether radical species form during Cyt*c* oxidation by Spn-H_2O_2, pneumococcal strains TIGR4, EF3030, their Δ*spxB*Δ*lctO* mutants, and a complemented strain (Ω*spxB-lctO*) were cultured in THY medium. Supernatants were combined with Cyt*c* and the spin trap DEPMPO [5-(Diethoxyphosphoryl)-5-methyl-1-pyrroline-N-oxide, 98%], and radical formation was monitored using continuous wave electron paramagnetic resonance (EPR). EPR spectra from TIGR4, TIGR4Ω*spxB-lctO*, and EF3030 supernatants with Cyt*c* were identical (Fig. 1G), indicating tyrosyl radical formation from Cyt*c* oxidation. No EPR signal was detected in Δ*spxB*Δ*lctO* mutant supernatants or wild-type cultures treated with catalase. The observed EPR spectra are consistent with both protein-attached and free-solution carbon-centered radicals. Spn strains TIGR4 and EF3030 induce significantly elevated intracellular ROS levels in lung epithelial cells compared to their isogenic Δ*spxB*Δ*lctO* mutants or mock-infected controls (45, 46), supporting a link between extracellular tyrosyl radical formation and intracellular oxidative stress.

***S. pneumoniae*-derived H_2O_2 contributes to mitochondrial aggregation and apical migration within alveolar cells.** Disruption of soluble Cyt*c* increases reactive oxygen species (ROS) production and triggers apoptotic cell death, which can induce mitochondrial morphological changes through fusion or fission events, altering organelle structure by combining or dividing mitochondria, respectively (47). To investigate the impact of Spn

infection on mitochondrial structure, human alveolar A549 cells were infected with pneumococcal strains TIGR4, EF3030, and their Δ*spxB*Δ*lctO* mutants for 8 h. Cells were stained for mitochondria (green), DNA (blue), and actin (red), and analyzed by confocal microscopy (Fig. 2).

In mock-infected control A549 cells, mitochondria exhibited a well-developed, interconnected network of elongated, filamentous structures surrounding the nuclei, characteristic of healthy, actively respiring cells (Fig. 2A). In contrast, both TIGR4-, and TIGR4Δ*spxB*Δ*lctO*-infected alveolar cells displayed fragmented and punctate mitochondria with a diffuse cytoplasmic distribution. These mitochondria were significantly smaller than those in mock-infected cells and exhibited irregular morphologies (Fig. 2A).

At different magnifications, A549 cells infected with Spn wild-type strains TIGR4 or EF3030 exhibited rounding and aggregation, with clusters of mitochondria forming around the nuclei (Fig. 2B, arrows). A more pronounced aggregation of mitochondria was apparent in EF3030-infected cells (Fig. 2B, arrows). Three-dimensional imaging analysis revealed that these mitochondrial clusters were predominantly localized on the apical surface of the infected cells (Fig. 2B and 2C). In contrast, mitochondria in TIGR4Δ*spxB*Δ*lctO*- and EF3030Δ*spxB*Δ*lctO*-infected alveolar cells appeared unevenly distributed, with varying sizes and intensities, suggesting aggregation around certain areas, near the nuclei or in regions of cellular stress (Fig. 2B and 2C). Similar mitochondrial aggregation was observed in human bronchial Calu-3 cells infected with Spn strains (Fig. S1).

Employing three-dimensional analysis, we categorized mitochondria in mock-infected and Spn-infected cells based on their spatial proximity to the apical surface. Mitochondria located within 5 µm of the cell surface were classified as 'apical,' while those positioned deeper

within the cellular architecture were designated as 'middle-bottom' (Fig. 2D). Quantitative assessment revealed that the area of mitochondrial aggregates at the apical side of TIGR4- and EF3030-infected alveolar epithelial cells (Fig. 2E) was significantly greater than that observed in mock-infected cells or cells infected with hydrogen peroxide-deficient knockout mutants (Fig. 2F and 2G) highlighting the impact of Spn-H_2O_2 on mitochondrial clustering and distribution. Taken together, these results indicate that Spn-derived H_2O_2 induces mitochondrial aggregation and apical migration in infected alveolar cells, likely exacerbating oxidative stress by disrupting mitochondrial dynamics.

***S. pneumoniae* inhibits mitochondrial respiration in host cells.** To investigate the impact of Spn-H_2O_2 on mitochondrial respiration, we employed an *ex vivo* model of infection. Rat heart mitochondria were isolated and subsequently incubated with supernatants from TIGR4, EF3030, or its H_2O_2-deficient mutant, Δ*spxB*Δ*lctO*, following 4 hours of growth in THY. Hydrogen peroxide levels in the supernatants were then quantified. Strain TIGR4 produced a median H_2O_2 concentration of 499.5 µM, while EF3030 secreted 1,119 µM H_2O_2 into the supernatant (Fig. 3A). The H_2O_2 levels in the supernatants of the mutant derivatives were significantly lower (<8.86 µM) (Fig. 3A).

Oxygen consumption, a proxy for electron transference through CIDR, or complex-II driven respiration (CIIDR) (Fig. 3B), was investigated using a high-resolution Oroboros O2k FluoRespirometer. Isolated mitochondria were treated with the TCA cycle substrates glutamate and malate to generate NADH and initiate CIDR, which facilitates the transfer of electrons through complexes I, III, and IV (Fig. 3B). Alternatively, mitochondria were treated with succinate to drive electron transfer through CIIDR (29, 33) (Fig. 3B). Notably, mitochondrial

CIDR was significantly inhibited by supernatants from TIGR4 at 5 µM H_2O_2, with maximal inhibition of mitochondrial respiration observed at concentrations ≥12.5 µM (Fig. 3C). In contrast, CIIDR was not inhibited by TIGR4 cultures containing the lowest H_2O_2 concentration, but statistically significant inhibition occurred at concentrations ≥25 µM (Fig. 3D). The factor in the supernatant causing the inhibition of mitochondrial respiration was Spn-H_2O_2, as an equivalent volume of supernatant from the TIGR4Δ*spxB*Δ*lctO* mutant did not inhibit CIDR, whereas the supernatant from the complemented strain caused CIDR inhibition (Fig. 3E). A comparison of residual CIDR and CIIDR activity revealed a marked difference between mock-infected and TIGR4-treated mitochondria. Mitochondria exposed to TIGR4 cultures exhibited ~10% of the CIDR activity observed in the mock-infected control, while CIIDR activity remained significantly higher (Fig. 3F). These findings suggest that Spn-H_2O_2 targets complex I, the NADH dehydrogenase complex, or TCA cycle enzymes involved in NADH synthesis.

To determine whether Spn-H_2O_2-mediated inhibition of CIDR is reversible or irreversible, we performed a catalase rescue assay and an *in vitro* reduction treatment. Incubating TIGR4-treated mitochondria with catalase fully restored CIDRy (Fig. 3G), whereas treating mitochondria exposed to Δ*spxB*Δ*lctO* supernatant with exogenous H_2O_2 significantly reduced CIDR (Fig. 3H, 3I). Furthermore, exogenous H_2O_2 treatment inhibited CIDR in these mitochondria (Fig. 3J). These results indicate that Spn-H_2O_2-induced inhibition of CIDR reversible and redox-sensitive, rather than resulting from irreversible oxidative damage.

***Streptococcus pneumoniae*-mediated inhibition of mitochondrial respiration occurs independently of electron transport chain activity.** To further investigate the impact of Spn on mitochondrial function, we assessed the oxidative activity of individual complexes within the

ETC. This was achieved by measuring the activity of each complex in mitochondria exposed to either sterile bacterial culture medium (mock) or supernatants from Spn strains TIGR4 and EF3030. Notably, no significant differences were observed in the oxidative capacity of complex I for its substrate NADH (Fig. 3K), or in the activity of any other ETC complexes, between mitochondria exposed to bacterial culture medium and those exposed to Spn supernatants (Fig. S2A-C). Therefore, inhibition of mitochondrial respiration by Spn occurs upstream the ETC.

***S. pneumoniae* H_2O_2-mediated inhibition of TCA cycle enzymes downstream of malate dehydrogenase in mitochondrial respiration.** Our results demonstrate that NADH, the substrate for complex I, can be oxidized sustaining mitochondrial respiration in the presence of Spn cultures (Fig. 3K). However, when mitochondria are supplemented with TCA cycle substrates that generate NADH, Spn cultures inhibit respiration. These findings led us to hypothesize that Spn-H_2O_2 selectively oxidizes TCA cycle enzymes, thereby impairing NADH production. To assess this, we stimulated cellular oxygen consumption in CIDR with a panel of TCA cycle substrate mixtures: pyruvate and malate, glutamate and malate, or succinate alone (Fig. 4A). It is well established that the substrate combinations optimize electron flow into complex I enhancing OXPHOS capacity (48). Mitochondrial respiration driven by substrates pyruvate and malate was not significantly inhibited by cultures of Spn (Fig. 4B). Similarly, cellular oxygen consumption stimulated by incubation with succinate (via complex II) was unaffected by cultures of the pneumococcus. Conversely, Spn strains TIGR4 and EF3030 significantly inhibited mitochondrial respiration induced by glutamate and malate (Fig. 4B). This data supports the hypothesis that Spn cultures inhibit enzymes of the TCA cycle, specifically

downstream of citrate synthase (CS), which catalyzes the irreversible conversion of acetyl-CoA and oxaloacetate to citrate leading to citrate accumulation in TIGR4-infected Calu-3 cells, consistent with findings by Surabhi et al. (2021)(49).

β-oxidation of medium-chain and long-chain fatty acids in the mitochondrial matrix produces acetyl-CoA, via electron transfer flavoprotein (ETF, Fig. 4B), which reacts with oxaloacetate to form citrate in the TCA cycle. We assessed whether supplementing oleate (long-chain) or octanoate (medium-chain) to isolated mitochondria incubated with Spn cultures inhibits CIDR. Compared to the mock control, cultures of both strains significantly inhibited CIDR (Fig. 4C), further indicating that the inhibition induced by Spn cultures occurs at or downstream of CS.

In the mitochondria, aconitase (ACO2) is located downstream of CS and catalyzes the reversible isomerization of citrate to isocitrate. The resulting isocitrate is then decarboxylated to α-ketoglutarate by isocitrate dehydrogenase 3 (IDH3A) (Fig. 4A). Glutamate in the mitochondria is converted to α-ketoglutarate by glutamate dehydrogenase (GDH), which is then decarboxylated to succinyl-CoA by α-ketoglutarate dehydrogenase (OGDHC) (Fig. 4A). We assessed the activity of ACO2, GDH, and OGDHC in isolated mitochondria exposed to cultures of Spn strains producing H_2O_2, comparing them to mock-infected conditions and to cultures of Δ*spxB*Δ*lctO* mutants. Both TIGR4 and EF3030, caused a significant inhibition of the enzymatic activity of ACO2 (Fig. 4D), GDH (Fig. 4E), and OGDHC (Fig. 4F), compared to mock-infected cultures or cultures of isogenic Δ*spxB*Δ*lctO* mutants.

To elucidate the mechanism of inhibition, sulfenic acid (RSOH) formation, a marker of cysteine oxidation, was assessed in human bronchial epithelial Calu-3 cells using DCP-Rho1 (26, 50) (Fig. 4J), a dimedone-based fluorogenic probe specific for RSOH (50) (Fig. 4K). Cells

infected with wild-type EF3030 exhibited significantly elevated RSOH levels in cytosolic (Fig. 4L, 4M), and mitochondrial (Fig. 4N) fractions compared to mock-infected cells or those infected with the H_2O_2-deficient Δ*spxB*Δ*lctO* mutant. These results indicate that Spn-H_2O_2 induces oxidative modification of cysteine residues in TCA cycle enzymes (ACO2, GDH, OGDHC), contributing to their inhibition. To further validate these findings in the same host cell model, we measured GDH activity in Calu-3 cells, either mock-infected or infected with Spn. Consistent with the *ex vivo* data, GDH activity in Spn-infected Calu-3 cells was significantly reduced compared to mock-infected controls or cells infected with Δ*spxB*Δ*lctO* (Fig. 4G), supporting the notion that Spn-H_2O_2 directly inhibits GDH, disrupting the TCA cycle and driving metabolic reprogramming in lung epithelial cells.

Spn-mediated transcriptional regulation of mitochondrial genes in lung cells. RNA sequencing (RNAseq) analysis of bronchial Calu-3 cells, a differentiated lung epithelial model derived from adenocarcinoma, revealed extensive transcriptional reprogramming following infection with TIGR4. Compared to mock-infected controls, TIGR4 infection dysregulated 2,684 genes (FDR <0.05, log2 fold change >0.5), a response largely driven by SpxB, as infection with the isogenic TIGR4Δ*spxB* mutant dysregulated only 163 genes (Fig. S3A and S3B). Gene ontology (GO) analysis indicated that TIGR4 infection induces a broad stress response, with significant enrichment of pathways related to DNA damage response, cell cycle regulation, and mitochondrial function (Fig. S3C and S3D). In contrast, TIGR4Δ*spxB* infection elicited a narrower response, primarily involving NF-κB signaling and apoptosis pathways. Notably, TIGR4 infection dysregulated 237 mitochondrial-related genes (GO:0005739), compared to a few in TIGR4Δ*spxB*-infected cells, highlighting SpxB's critical role in mitochondrial gene

regulation (Table S1). Calu-3 cells, exhibiting a metabolic profile less dependent on Warburg metabolism than more aggressive cancer cell lines, provide a physiologically relevant model for studying epithelial responses to bacterial infection (51).

Among the dysregulated genes, TIGR4 infection significantly upregulated IDH3A (isocitrate dehydrogenase 3) and PDK1 (pyruvate dehydrogenase kinase 1) RNA expression in Calu-3 cells (Fig. 4H), while downregulating PC (pyruvate carboxylase), PDK2 (pyruvate dehydrogenase kinase 2), and PDPR (pyruvate dehydrogenase phosphatase regulatory subunit). The proteins encoded by these genes regulate the pyruvate dehydrogenase complex (PDC), which controls pyruvate entry into the mitochondrial TCA cycle. Upregulation of PDK1 likely inhibits PDC activity, while concurrent downregulation of PDK2 and PDPR further suppresses PDC function, potentially limiting mitochondrial oxidative phosphorylation and mitigating oxidative stress. This pattern was absent in TIGR4Δ*spxB*-infected cells, which lack pyruvate oxidase and H_2O_2 production. However, a similar dysregulation was observed with the H_2O_2-producing TIGR4Δ*lctO* mutant (Fig. 4H), emphasizing SpxB-mediated oxidative stress in driving these changes.

Supporting SpxB-driven transcriptional reprogramming, genes encoding oxidative stress response enzymes, including SOD2 (superoxide dismutase 2), TXNRD1 (thioredoxin reductase 1), HMOX1 (heme oxygenase 1), and NFKB1 (nuclear factor kappa B subunit 1), were upregulated in Calu-3 cells infected with TIGR4 and TIGR4Δ*lctO* (Fig. 4I). Expression remained unchanged in TIGR4Δ*spxB*-infected cells, highlighting SpxB's role in eliciting a robust antioxidant defense. Similar dysregulation of PDK1 and SOD genes was observed in non-cancerous bronchial BEAS-2B cells infected with Spn strain D39 (52) (explained later, Fig. 7E).

Spn-H_2O_2-driven metabolic reprogramming in lung epithelial cells. Inhibition of key TCA cycle enzymes, including ACO2, and OGDHC, by Spn may lead to citrate accumulation in host cells. To investigate this, intracellular and extracellular citrate concentrations were measured in mock-infected Calu-3 bronchial epithelial cells and compared to cells infected with Spn strains TIGR4 or TIGR4Δ*spxB*Δ*lctO* for 8 h. Extracellular citrate levels, quantified by high-performance liquid chromatography (HPLC), were significantly elevated in TIGR4- and TIGR4Δ*spxB*Δ*lctO*-infected cells (median 227 µM and 441 µM, respectively) compared to mock-infected controls (4.04 µM) (Fig. 5A). Citrate levels in Spn culture supernatants (without host cells) were comparable between TIGR4 and TIGR4Δ*spxB*Δ*lctO*, suggesting bacterial contribution to extracellular citrate (Fig. 5A). However, intracellular citrate concentrations were significantly higher in TIGR4-infected cells compared to mock-infected or TIGR4Δ*spxB*Δ*lctO*-infected cells (Fig. 5B), indicating that H_2O_2-producing Spn exacerbates mitochondrial citrate accumulation, likely due to TCA cycle inhibition. This citrate accumulation in TIGR4-infected Calu-3 cells aligns with findings by Surabhi et al. (2021)(49), confirming that Spn-H_2O_2-mediated TCA cycle inhibition is a key driver of metabolic reprogramming in infected host cells.

Metabolite analysis revealed that Spn infection enhances glucose consumption. Baseline glucose in Calu-3 cells was 1.8 g/L, decreasing to 1.2 g/L in mock-infected cells after 8 h. In TIGR4- and TIGR4Δ*spxB*Δ*lctO*-infected cells, glucose levels dropped below 0.16 g/L (Fig. 5C), while Spn cultures alone consumed less than 0.65 g/L, indicating a host-specific response likely driven by SpxB-mediated oxidative stress and TCA cycle suppression. Acetate production, absent in mock-infected cells, increased to 4.54 mM in TIGR4-infected cells but was lower in TIGR4Δ*spxB*Δ*lctO*-infected cells (1.58 mM) (Fig. 5E). Spn cultured alone

347 produced 2.35 mM (TIGR4) and 0.29 mM (TIGR4Δ*spxB*Δ*lctO*) acetate, reflecting SpxB's role
348 in acetate synthesis via acetyl phosphate under aerobic conditions (Fig. 5D). Lactate levels
349 further highlighted metabolic shifts. Extracellular lactate in mock-infected cells was 1.96 mM,
350 increasing to 8.9 mM (TIGR4) and 8.4 mM (TIGR4Δ*spxB*Δ*lctO*) in infected cells, with Spn
351 alone producing 4.7 mM (TIGR4) and 6.3 mM (TIGR4Δ*spxB*Δ*lctO*) (Fig. 5F). Intracellular
352 lactate, 1.17 mM in mock-infected cells, decreased significantly in infected cells, likely due to
353 Spn-induced cytotoxicity (Fig. 5G). RNA-seq analysis revealed significant upregulation of
354 glycolysis-related genes in TIGR4-infected cells, including IER3, DDIT4, HK2, HIF1A, and
355 PFKP ($\log_2$ fold change 1–4, FDR <0.05), with IER3, HK2 and PFKP also upregulated in
356 TIGR4Δ*lctO*-infected cells (Fig. 5H, 5J). IER3 (immediate early response 3) and HIF1A
357 (hypoxia-inducible factor 1-alpha) transcriptionally regulates glycolytic genes glycolytic genes
358 promoting a Warburg-like glycolytic shift in cancer cells (53, 54). Similarly, RNA-seq analysis of
359 BEAS-2B bronchial epithelial cells infected with Spn for 9 or 16 h revealed upregulated
360 expression of glycolysis-related genes HK2, PDK1, TK2, PFKFB3, and IER3 (Fig. 5I). These
361 findings in a non-cancerous cell line corroborate the Warburg-like glycolytic shift observed in
362 Calu-3 cells. In TIGR4Δ*spxB*-infected cells, most genes were unchanged except for HK2,
363 BPGM, and HIF1A, underscoring SpxB-H_2O_2's role in glycolytic reprogramming.

364 Collectively, Spn-H_2O_2 induces profound metabolic reprogramming in Calu-3 cells,
365 marked by citrate accumulation, enhanced glucose consumption, increased extracellular
366 lactate and acetate, and selective upregulation of glycolytic genes, reflecting a host response
367 to SpxB-mediated mitochondrial impairment.

368

369 **Infection with *S. pneumoniae* does not cause loss of alveolar mitochondrial membrane**
370 **potential.** Increased permeability of the mitochondrial inner membrane (IMM) can dissipate

the proton electrochemical gradient and destabilize mitochondrial membrane potential (ΔΨm), both of which are essential for ATP synthesis via ATP synthase. Given that Spn-H_2O_2 inhibits the TCA cycle, we hypothesized that enhanced mitochondrial permeability contributes to this effect. To test this, ΔΨm—established primarily by proton translocation through complexes I, III, and IV of the electron transport chain (ETC)—was assessed, as it, together with the proton gradient, constitutes the proton-motive force driving ATP production (55). In healthy mitochondria, ΔΨm is tightly regulated; its dissipation or reduction signals impaired ATP synthesis, mitochondrial dysfunction, and increased reactive oxygen species (ROS) production. Here, we evaluated the impact of Spn-derived H_2O_2 on ΔΨm in A549 alveolar epithelial cells using flow cytometry with the potentiometric dye JC-1.

In cells with intact mitochondrial function, the cell-permeant dye JC-1 accumulates in polarized mitochondria, forming aggregates that exhibit a balanced fluorescence emission profile, with an approximately equal ratio of Texas Red (~590 nm) to FITC (~530 nm). This dual-emission state is detected as a +Texas Red/+FITC double-positive population in flow cytometry, indicative of robust ΔΨm. Consistent with this, uninfected A549 cells stained with JC-1 displayed this characteristic pattern, reflecting maintained ΔΨm (Fig. 6A). In contrast, treatment with carbonyl cyanide m-chlorophenyl hydrazone (CCCP), a known ΔΨm uncoupler, induced complete depolarization, shifting the population to -Texas Red/+FITC single-positive cells (Fig. 6B).

To assess the effects of Spn-derived H_2O_2 on mitochondrial function, A549 cells were infected with wild-type strains TIGR4 and EF3030, or their respective H_2O_2-deficient mutants TIGR4Δ*spxB*Δ*lctO* and EF3030Δ*spxB*Δ*lctO*. ΔΨm was then quantified using JC-1 staining and flow cytometry. Relative to the CCCP-treated positive control, which induces complete ΔΨm

394 dissipation by enhancing proton permeability across the IMM, infections with TIGR4 and
395 EF3030 resulted in significantly less mitochondrial depolarization (Figs. 6D, 6G, 6I). Similarly,
396 treatment of A549 cells with 2 mM H_2O_2 alone did not alter ΔΨm (Fig. 6C), suggesting that
397 H_2O_2 at this concentration does not directly impair mitochondrial membrane integrity.
398 Furthermore, A549 cells infected with TIGR4 or EF3030 and subsequently treated with CCCP
399 exhibited complete ΔΨm dissipation (Figs. 6F, 6G, 6I), confirming that lung epithelial cells
400 maintain an intact ΔΨm despite Spn infection over this timeframe. No significant changes in
401 ΔΨm were observed in cells infected with TIGR4Δ*spxB*Δ*lctO* or EF3030Δ*spxB*Δ*lctO* compared
402 to their wild-type counterparts, indicating that Spn-derived H_2O_2 does not substantially affect
403 ΔΨm under these conditions.

404 To evaluate cytotoxicity, the same population of infected A549 cells was analyzed using
405 SYTOX Blue staining and flow cytometry. Compared to mock-infected controls, no significant
406 reduction in cell viability was observed in A549 cells infected with TIGR4 or its H_2O_2-deficient
407 mutant TIGR4Δ*spxB*ΔlctO (Fig. 6H). In contrast, infection with EF3030 resulted in a significant
408 decrease in cell viability relative to mock-infected controls and the corresponding H_2O_2-
409 deficient mutant EF3030Δ*spxB*Δ*lctO* (Fig. 6J), likely due to elevated H_2O_2 production by
410 EF3030 relative to TIGR4 (Fig. 3A). Collectively, these results suggest that Spn infection does
411 not substantially impair ΔΨm, consistent with H_2O_2 targeting TCA cycle enzymes (e.g., ACO2,
412 OGDHC) rather than ETC complexes, thereby preserving mitochondrial membrane integrity
413 over the experimental timeframe.

414

415 **Spn-Derived H_2O_2 modulates limited alveolar apoptosis via TCA cycle Inhibition.** Having
416 demonstrated that Spn-derived H_2O_2 inhibits the tricarboxylic acid (TCA) cycle without

disrupting mitochondrial membrane potential (ΔΨm) in lung epithelial cells, we explored whether this metabolic perturbation triggers cell death by impairing oxidative phosphorylation (OXPHOS). Apoptosis was evaluated using the terminal deoxynucleotidyl transferase biotin-dUTP nick end labeling (TUNEL) assay, which detects DNA fragmentation—a characteristic of late-stage apoptosis—by fluorescently labeling 3'-OH termini in fragmented DNA, facilitating quantitative analysis of apoptotic cell populations via confocal microscopy. Additionally, activation of caspase-3 and caspase-7 was assessed using flow cytometry and confocal microscopy. Mock-infected A549 alveolar epithelial cells displayed minimal DNA fragmentation, whereas DNase I-treated cells, serving as a positive control, exhibited a marked increase in fluorescence intensity, predominantly localized to nuclear regions (Fig. 7A, Fig. S4A), validating the assay. Cells treated with staurosporine, a known apoptosis inducer, showed reduced viability, with ~60% of viable cells exhibiting activated caspase-3/7 (Fig. 7C). Three-dimensional reconstruction of z-stacks, including XY, XZ, and YZ optical sections (Fig. 7E, Fig. S5), along with time-lapse microscopy (Video S1), confirmed apoptosis induction in staurosporine-treated cells.

A549 cells were infected for 10 h with wild-type Spn strains TIGR4 and EF3030, or their H_2O_2-deficient mutants TIGR4Δ*spxB*Δ*lctO* and EF3030Δ*spxB*Δ*lctO*. TUNEL-positive cells were observed infrequently across all infected conditions (Fig. 7A, Fig. S4), though the signal in infected cells was significantly higher than in mock-infected controls (Fig. 7B, Fig. S4B), yet markedly lower than in DNase I-treated cells. Notably, cells infected with H_2O_2-producing strains TIGR4 and EF3030 exhibited a significantly greater TUNEL signal compared to those infected with H_2O_2-deficient mutants (Fig. 7B, Fig. S4B), indicating that Spn-derived H_2O_2 promotes cell death. Consistent with this, flow cytometry analyses revealed a significantly

440 greater proportion of viable cells in infections with H_2O_2-deficient mutants compared to their
441 wild-type counterparts (Fig. 7D). However, activation of caspase-3/7 in Spn-infected cells was
442 not detected at 10 h post-infection, as confirmed by flow cytometry, confocal microscopy and
443 time-lapse studies (Fig. 7C, 7F, Fig. S4C, Fig. S5 and Video S1). These findings suggest that
444 H_2O_2-mediated inhibition of TCA cycle enzymes (e.g., ACO2, OGDHC), which supply electron
445 donors for OXPHOS, contributes to a limited apoptotic response, consistent with the minimal
446 ΔΨm disruption observed previously.

447 To further explore the role of H_2O_2 in apoptosis, A549 cells were treated with 2 mM
448 H_2O_2 every 2 h for 8 h, simulating the delayed accumulation of Spn-derived H_2O_2 during
449 infection, which becomes detectable after 4 hours as cellular substrates are depleted (46).
450 TUNEL analysis revealed that the apoptotic signal in H_2O_2-treated cells was comparable to
451 that in wild-type Spn-infected cells but significantly lower than in DNase I-treated controls (Fig.
452 7A, 7B). These results confirm that Spn-derived H_2O_2 contributes to limited alveolar cell
453 apoptosis, likely via metabolic stress from TCA cycle inhibition, though its effect is less
454 pronounced than that of canonical apoptosis inducers.

455 Gene expression analysis revealed a complex interplay of apoptosis regulation in
456 human bronchial cells infected with H_2O_2-producing strains TIGR4 and TIGR4Δ*lctO* compared
457 to mock-infected controls and the H_2O_2-deficient mutant TIGR4Δ*spxB* (Fig. 7G). Pro-apoptotic
458 genes, including FAS and BBC3, were significantly upregulated in TIGR4-infected cells ($\log_2$
459 fold-change [FC] 1–6; FDR < 0.05), promoting apoptosis via death receptor signaling and
460 stress response pathways. Concurrently, anti-apoptotic genes such as BCL2A1 (BCL2-family
461 member, prevent Cyt*c* release) and TRAF1 were also upregulated, likely counteracting cell
462 death by inhibiting caspase activation and enhancing survival through NF-kappaB signaling

(NFKB1). This dual upregulation of pro- and anti-apoptotic genes, absent in TIGR4Δ*spxB*-infected cells, likely underlies the limited apoptosis observed in the TUNEL assay, as the balance between these opposing pathways mitigates extensive cell death despite *spxB*-mediated H_2O_2 stress. Similar dual regulation of pro- and anti-apoptotic genes was observed in BEAS-2B cells infected with Spn reference strain D39 for 16 hours (Fig. 7H), mirroring patterns reported in MYC-driven cancer biology (56). These findings highlight a novel mechanism by which Spn modulates host cell survival to sustain infection.

Discussion

This study unveils a novel and unique mechanism by which Spn disrupts host cell metabolism through H_2O_2-mediated inhibition of the TCA cycle, coupled with extensive transcriptional and metabolic reprogramming in lung epithelial cells. To our knowledge, direct inhibition of the TCA cycle enzymes by a bacterial pathogen has not been described prior to this work, positioning Spn's H_2O_2-driven metabolic disruption as a groundbreaking insight into pneumococcal pathogenesis. Spn-derived H_2O_2, primarily produced by pyruvate oxidase (SpxB), targets key mitochondrial enzymes—aconitase (ACO2), glutamate dehydrogenase (GDH), and α-ketoglutarate dehydrogenase (OGDHC)—significantly inhibiting their activities. H_2O_2-induced cysteine oxidation, marked by elevated sulfenic acid levels in EF3030-infected Calu-3 cells, drives this inhibition. This leads to citrate accumulation, as evidenced by elevated intracellular and extracellular citrate levels in TIGR4-infected Calu-3 cells compared to mock-infected controls or cells infected with the H_2O_2-deficient mutant TIGR4Δ*spxB*Δ*lctO*. This H_2O_2-driven citrate accumulation, also observed by Surabhi et al. (2021)(49), highlights Spn's unique strategy to disrupt host metabolism via TCA cycle inhibition

This metabolic bottleneck downstream of citrate synthase impairs NADH production and succinate reduction, critical electron donors for OXPHOS, aligning with the observed inhibition of CIDR at H_2O_2-concentrations as low as 5 µM. In contrast, CIIDR, which utilizes substrates acting downstream of the enzymes inhibited by Spn-H_2O_2, required higher concentrations (25 µM) for inhibition. Catalase rescue and exogenous H_2O_2 treatment assays (Fig. 3G–3J) revealed that Spn-H_2O_2-mediated inhibition of CIDR is reversible and redox-sensitive, suggesting dynamic modulation of mitochondrial function. This reversibility highlights potential therapeutic strategies to mitigate Spn-induced metabolic stress by targeting redox pathways. Notably, the absence of significant changes in ETC complex activities (Fig. 3K, Fig. S2) underscores that Spn-H_2O_2 targets upstream TCA cycle enzymes rather than the ETC itself, a mechanism distinct from the ETC decline associated with human diseases like neurodegeneration, cancer, and diabetes (57).

The hallmark of pneumococcal disease is Spn's ability to invade host cells and manipulate their metabolism to establish infection (58). Our findings demonstrate that H_2O_2-mediated inhibition of the TCA cycle disrupts host energy metabolism and induces transcriptional reprogramming, shifting lung epithelial cells toward a Warburg-like phenotype(59) that fosters bacterial proliferation. The NAD^+ salvage pathway, which supplies electron donors for host antibacterial responses against Spn (52), is likely impaired by reduced NADH production resulting from TCA cycle suppression. This metabolic disruption compromises host defenses, enabling Spn to exploit host resources, as evidenced by significant glucose depletion in TIGR4-infected Calu-3 cells. Furthermore, transcriptional reprogramming in TIGR4-infected cells amplifies this metabolic shift. Upregulation of glycolysis-associated genes (HK2, PFKP, HIF1A) and downregulation of pyruvate

509 dehydrogenase complex regulators (PC, PDK2, PDPR) indicate the Warburg-like metabolic
510 switch toward glycolysis (59), likely a compensatory response to H_2O_2-induced mitochondrial
511 dysfunction. To further validate the Warburg-like metabolic shift in a non-cancerous context,
512 RNA-seq analysis of BEAS-2B bronchial epithelial cells infected with Spn strain D39 (Fig. 5I)
513 confirmed upregulated expression of glycolysis-related genes (HK2, PDK1, TK2, PFKFB3) and
514 IER3, reinforcing the physiological relevance of these transcriptional changes across cell types
515 (52). This reprogramming, absent in TIGR4Δ*spxB*Δ*lctO*-infected cells, underscores the critical
516 role of SpxB in driving host metabolic stress.

517 Spn- H_2O_2 induces mitochondrial aggregation and apical migration in A549 cells (Fig.
518 2B–C) and Calu-3 cells (Fig. S1), indicative of disrupted mitochondrial dynamics that amplify
519 oxidative stress. The interaction between the cytoskeleton and the mitochondrial outer
520 membrane is critical for regulating mitochondrial respiration (60). Mutations in microtubule-
521 associated proteins, such as plectin or desmin, impair mitochondrial network integrity, and
522 similarly, Spn-H_2O_2-mediated microtubule disruption, absent in H_2O_2-deficient mutants (17, 23),
523 likely drives mitochondrial aggregation and mislocalization in lung epithelial cells, potentially
524 contributing to metabolic dysfunction. Supporting this, the absence of βII-tubulin in
525 cardiomyocytes correlates with a shift to glycolysis-dependent metabolism (Warbug effect)
526 (61). The increased extracellular lactate and acetate in TIGR4-infected cells (Fig. 5E–F)
527 reflect Spn's manipulation of host glycolytic flux, potentially fueling bacterial metabolism while
528 stressing host cells. Notably, mitochondrial membrane potential (ΔΨm) remains intact in
529 TIGR4- and EF3030-infected cells, indicating that H_2O_2 targets TCA cycle enzymes rather than
530 ETC complexes or membrane integrity. The preservation of mitochondrial membrane potential
531 (ΔΨm) in TIGR4- and EF3030-infected cells (Fig. 6) reflects the selective inhibition of TCA

cycle enzymes by Spn-H_2O_2, rather than ETC damage, as exogenous H_2O_2 might cause (62). This distinction underscores the physiological relevance of our infection model, where H_2O_2 levels (499.5–1,119 µM) target upstream metabolic pathways. This preservation of $\Delta\Psi m$ aligns with the limited apoptosis observed in TUNEL assays, where TIGR4- and EF3030-infected cells showed significantly higher apoptotic signals than H_2O_2-deficient mutants but far less than DNase I-treated controls. The balanced upregulation of pro-apoptotic (FAS, BBC3) and anti-apoptotic (BCL2A1, TRAF1) genes in TIGR4-infected cells likely mitigates extensive cell death, enabling Spn to maintain host cell viability for sustained infection.

The decline in ETC activity is a hallmark of many human diseases, yet our study uniquely demonstrates that Spn directly targets the TCA cycle, upstream of the ETC, to disrupt host metabolism. The oxidation of soluble Cyt*c* by Spn-H_2O_2, forming tyrosyl radicals, further impairs mitochondrial function by disrupting electron transfer, amplifying ROS production, and exacerbating metabolic stress. This mechanism not only enhances Spn's virulence but also parallels metabolic disruptions, suggesting broader implications for understanding host-pathogen interactions. Elevated intracellular ROS levels in lung epithelial cells infected with wild-type Spn strains TIGR4 and EF3030, compared to Δ*spxB*Δ*lctO* mutants or mock-infected controls, support a mechanistic link between extracellular tyrosyl radical formation and intracellular oxidative stress, amplifying mitochondrial dysfunction (45, 46).

While heart mitochondria provided a robust model for studying Spn-induced mitochondrial dysfunction in this study, their physiological differences from lung epithelial mitochondria, including substrate preference (fatty acids vs. glucose/glutamine) and higher respiratory capacity, may limit direct extrapolation to the lung context. These differences, coupled with distinct ROS handling capacities in lung epithelial mitochondria, suggest that

tissue-specific responses to Spn-H_2O_2 may vary. Future studies using mitochondria isolated from lung epithelial cells could validate our findings and elucidate tissue-specific metabolic responses to Spn infection, enhancing the translational relevance of our results.

In conclusion, Spn employs H_2O_2-mediated inhibition of the TCA cycle as a novel strategy to reprogram host cell metabolism and the transcriptional profiles, thereby facilitating bacterial invasion and persistence. By disrupting NADH production and inducing glycolytic reprogramming, Spn impairs host antibacterial responses, including those dependent on the NAD^+ salvage pathway(52), while enhancing its own survival. These findings underscore the therapeutic potential of targeting SpxB activity, such as through SpxB inhibitors, or restoring TCA cycle function to attenuate pneumococcal disease severity. Recent evidence suggests that enhancing host cell NAD^+ metabolism can suppress Spn replication (52). Future studies should delineate the molecular interactions between H_2O_2 and TCA cycle enzymes, investigate the role of host antioxidant defenses in mitigating Spn-induced metabolic stress, and employ *in vivo* models to elucidate how Spn's metabolic manipulation drives disease progression. Such investigations may inform the development of innovative therapeutic strategies for pneumococcal infections.

Material and Methods

Bacterial strains, growth conditions, and preparation of inoculum. Spn strains utilized in this study are listed in Table 1. Strains were cultured on blood agar plates (BAP) containing 5% sheep's blood from frozen bacterial stocks stored in skim milk, tryptone, glucose, and glycerin (STGG)(63) or in Todd-Hewitt broth supplemented with 0.5% (w/v) yeast extract (THY) and incubated at 37°C with 5% CO_2. Inoculum for experiments was prepared as previously

578 described (9). Overnight cultures of Spn on BAP were harvested in phosphate buffered saline
579 (PBS) (pH 7.4), the OD_{600} of this suspension was obtained and adjusted to a final 0.1 density
580 that contained ~5.15 x 10^8 cfu/ml.

581 **Cell cultures.** A549 human type II alveolar epithelial cells (ATCC, CCL-185) were cultured in
582 Dulbecco's Modified Eagle's Medium (DMEM) (Gibco) supplemented with 10% fetal bovine
583 serum (FBS), 2 mM L-glutamine (Gibco), and 100 U/mL of penicillin-streptomycin (Gibco) in 25
584 cm^2 flasks (Fisher). Calu-3 cells (ATCC, HTB-55) were cultured in Eagle's Minimum Essential
585 Medium (EMEM, ATCC) supplemented with 10% FBS and 100 U/mL of penicillin-streptomycin
586 (Gibco). Cell passages were performed by trypsinization with Trypsin-EDTA (0.25%), phenol
587 red (Gibco). Cells were incubated at 37°C with 5% CO_2 and were supplemented with fresh
588 medium 2-3 times weekly and passaged to a new flask weekly or when cells reached ~100%
589 confluency.

590 **Infection of human bronchial and alveolar cells with *S. pneumoniae* strains.** Cell infection
591 experiments were performed using cells cultured for 8-10 days in the specified device. Cells
592 were grown in 6-well plates with glass cover slips (Genesee, Fisher) or 8-well glass slides
593 (Thermo Fisher Scientific, Nunc Lab-Tek II CC2) at 37°C with 5% CO_2. Prior to infection, cells
594 were washed three times with sterile PBS and then incubated in infection media consisting of
595 DMEM or EMEM, supplemented with 5% FBS, 2 mM L-glutamine (only DMEM), and 1X
596 HEPES (Gibco), referred as to infection medium. Cells were infected with Spn strains, mutant
597 derivatives, or along with appropriate controls, and incubated at 37°C with 5% CO_2 for various
598 time points.

599 **Cytochrome c Oxidation Assay.** To analyze the oxidation and degradation of heme in
600 cytochrome c (Cytc) by Spn-H_2O_2, THY supplemented with 56 µM Cytc from horse heart

(Sigma) was inoculated with Spn and incubated for 6 hours at 37°C with 5% CO2 in a 6-well plate. Supernatants were collected, centrifuged at 4°C for 5 minutes at 21,130×g, and transferred to a 96-well plate. The plate was then analyzed by spectroscopy, spanning wavelengths from 200 nm to 1000 nm, using an SYN H1 Hybrid Biotek reader (Agilent). As a control, 500 units (U) of catalase were added to a well containing THY-Cytc and Spn.

Detection of radicals by spin-trapping. DEPMPO [5-(Diethoxyphosphoryl)-5-methyl-1-pyrroline-N-oxide, 98%, Cayman Chemical, P/N 10006435] was utilized to detect and identify the formation of radical species. Spn was cultured in THY and incubated for 4 h at 37°C. As a control, uninfected THY was incubated in the same condition. After incubation, the cell suspension was micro-centrifuged, and 32 µL of supernatant was used for each spin-trapping sample. The final reaction mixture contained, when added, 30 mM DEPMPO and 56 µM Cyt*c*, in a volume of 40 µL. Spn-H_2O_2 free sample was obtained by pretreating the bacterial supernatant liquid with 100 U catalase for 1 minute. Methods of radical detection are performed as described previously(5).

Fluorescent staining of alveolar cells. A549 cells, or Calu-3 cells, seeded in a 6-well plate with glass coverslips were washed and added with infection media as mentioned above. Cells were then infected with Spn and incubated for 4, 6, or 8 h. After incubation with Spn, cells were fixed with 2% paraformaldehyde, permeabilized with 0.5% Triton X100, and blocked with 2% bovine serum albumin (BSA) following a previously described protocol(5). Post-blocking, cellular mitochondria were stained with an anti-mitochondria MTC02 monoclonal antibody (Invitrogen) at a concentration of 2 µg/mL in 2% BSA for 1 h. Cells were then washed with PBS and incubated for 1 h with a secondary goat anti-mouse FITC (SouthernBiotech) at a concentration of 20 µg/mL and phalloidin (7 units), or WGA-A555 at 1 µg/mL (ThermoFisher),

in 2% BSA for 1 h. Cells were then washed, the coverslips were removed from the wells, allowed to dry, mounted, and stained for DNA using ProLong Diamond antifade mountant containing DAPI (50 µg/mL). Slides were then imaged using a Nikon Eclipse C2 laser scanning confocal system mounted on a Ti-E motorized inverted microscope. Excitation/stimulation was performed with a solid state 405/488/561/640 laser unit using a CFI Apo 60X oil immersion objective, NA 1.40. Images were collected with a high sensitivity C2-DU3 Detection Unit with 435/34, 525/50, and 600/50 filters. Confocal images were analyzed using Imaris x64 software version 10.1.0.

Live cell imaging and time-lapse microscopy. A549 cells were seeded onto collagen-coated 35-mm glass-bottom dishes (MatTek) and cultured to confluence. Prior to infection, treatment, and imaging, cells were washed three times with PBS and incubated in infection medium supplemented with DAPI (50 µg/mL), wheat germ agglutinin–Alexa Fluor 555 (WGA-A555; 1 µg/mL), and CellEvent Caspase-3/7 Green Detection Reagent (2 µM; ThermoFisher). For apoptosis induction, cells were treated with staurosporine (1 or 10 µM; Sigma) for 7 h. For infection experiments, cells were exposed to Spn strains TIGR4 or EF3030 and incubated for 10 h at 37 °C in a humidified chamber (H301-Nikon-TI-S-ER) with 5% CO_2 maintained by an Okolab controller. Live-cell confocal imaging and time-lapse acquisition were performed using a Nikon Eclipse C2 laser scanning confocal microscope with the specifications described above. Image processing and analysis of both static and time-lapse datasets were conducted using Imaris software (x64, version 10.1.0).

Bulk RNA sequencing analysis. Human bronchial Calu-3 cells were seeded in 100 mm tissue culture treated dishes (Fisher) and incubate until they became polarized, 10-day post seeding. Cells were washed three times with sterile PBS and infected with Spn, mutant

derivatives, or mock-infected, and incubated for 4 h at 37°C in a 5% CO_2 atmosphere. After incubation, supernatant containing planktonic pneumococci were removed, the infected cells were harvested in one ml TRIzol (Invitrogen) and immediately flash frozen at -80°C. The following procedures were performed by the UMMC Molecular and Genomics Core Facility (www.umc.edu/genomicscore). RNA was extracted using the Pure Link RNA Mini Kit from archived samples (Invitrogen) according to manufacturer instructions and assessed for quality control parameters of minimum concentration and fidelity (i.e. 18S and 28S bands, RIS >8) through the UMMC Molecular and Genomics Core Facility (MGCF). Libraries were prepared for RNA sequencing per detailed protocols from Illumina mRNA stranded kit. Briefly, a pooled library was prepared from using n=12-24 samples per group using TruSeq mRNA Stranded Library Prep Kit (Set-A-indexes), quantified with the Qubit Fluorometer (Invitrogen), and assessed for quality and size Qiagen QIAxcel Advanced System or Agilent TapeStation. The library was sequenced using the NextSeq 2000 using P3 (200 cycles, paired end 100bp) on the Illumina NextSeq 2000 platform. Sequenced reads were assessed for quality using the Illumina BaseSpace Cloud Computing Platform and/or custom analysis pipeline and FASTQ sequence files were aligned reads to the reference genome (e.g., Ensembl/Hg38, Rnor_6.0, etc.) using DRAGEN RNA Pipeline Application (v.3.7.5) or custom analysis pipelines developed through MGCF. Differential expression was determined using DRAGEN Differential Expression Application (v.3.10.4) of DESeq2. Differentially expressed genes (DEGs) were identified using cutoffs of log2 (fold change) > 0.5 (~1.4-fold) and log2 (fold change) > 1 (2-fold), with an adjusted *p*-value < 0.05. Gene Set Enrichment Analysis was performed using Reactome analysis tools (https://reactome.org/) or other databases. Data was deposited into NCBI GEO data under accession number GSE301601.

Gene expression study deposited in NCBI-GEO (GSE195778)(52) was utilized to investigate the expression of genes in the D39 background. We focused on RNA data from human bronchial epithelial cell line BEAS-2B were infected with Spn at multiplicity of infection (MOI) of 1 for 9 or 16 h, and compared against the mock-infected control.

To elucidate the biological implications of Spn infection, functional enrichment analysis was performed on differentially expressed genes (DEGs) using DAVID (v2023q1) and g:Profiler (v.e109_eg56_p17). DAVID and g:Profiler were used to identify enriched Gene Ontology (GO) terms across three categories: Biological Process (BP), Molecular Function (MF), and Cellular Component (CC). In TIGR4-infected Calu-3 cells, GO-BP analysis revealed significant enrichment of terms related to "mitochondrial organization" (GO:0007005, FDR = 2.3e-04), "cellular response to oxidative stress" (GO:0034599, FDR = 8.7e-03), and "apoptotic process" (GO:0006915, FDR = 1.2e-02), consistent with Spn-H_2O_2-induced mitochondrial dysfunction and limited apoptosis. GO-CC terms highlighted "mitochondrial inner membrane" (GO:0005743, FDR = 4.5e-03) and "respiratory chain complex" (GO:0098803, FDR = 9.1e-03), aligning with the observed inhibition of CIDR. KEGG pathway analysis via DAVID identified downregulation of the TCA cycle pathway (hsa00020, FDR = 3.8e-03) in TIGR4-infected cells, corroborating the inhibition of TCA cycle enzymes like ACO2 and OGDHC, while the "Glycolysis/Gluconeogenesis" pathway (hsa00010, FDR = 1.1e-02) was upregulated, reflecting the enhanced glycolysis observed (e.g., HK2 upregulation). Complementary analysis using g:Profiler provided additional insights into molecular networks. The "oxidative phosphorylation" pathway (KEGG:00190, p-adj = 2.4e-03) was significantly downregulated in TIGR4-infected cells, consistent with CIDR inhibition, while "response to reactive oxygen species" (GO:0000302, p-adj = 5.6e-03) was enriched, supporting the upregulation of oxidative stress

response genes (SOD2, TXNRD2). Notably, in TIGR4Δ*spxB*Δ*lctO*-infected cells, these pathways showed minimal perturbation, underscoring the role of H_2O_2 in driving these changes.

Heart mitochondria isolation. Intact rat heart mitochondria were isolated from Sprague Dawley rats similar to published methods (64, 65). Mitochondria were isolated from rat heart tissue due to their higher yield and robust respiratory performance compared to lung epithelial mitochondria, enabling reliable and high-quality bioenergetic analyses. While heart mitochondria preferentially utilize fatty acids and exhibit higher respiratory capacity, lung epithelial mitochondria rely more on glucose and glutamine and may have distinct ROS handling properties. These differences were considered in the context of modeling mitochondrial responses to Spn infection, with the conserved respiratory machinery supporting the relevance of our findings. In brief, heart tissue was minced with a razor blade in 500 µL of MSM buffer (220 mM mannitol, 70 mM sucrose, 5 mM MOPS pH 7.4) supplemented with 2 mg/mL bacterial proteinase type XXIV. The minced tissue was added to 5 mL of ice-cold isolation buffer (MSM buffer supplemented with 2 mM EDTA and 0.2% fatty acid-free BSA) and homogenized on ice with a glass homogenizer and a Teflon pestle for 4 strokes. To inhibit the proteinase, 0.1 mM phenylmethylsulfonyl fluoride (PMSF) was used. The tissue homogenate was centrifuged at 300×g for 10 min at 4°C. The supernatant was then centrifuged at 3000×g for 10 min at 4 °C, and the mitochondrial pellet washed once in ice-cold MSM buffer. Protein concentration was determined by using the BioRad DC protein assay.

Hydrogen peroxide quantification. H_2O_2 levels were quantified from culture supernatants of different Spn strains. Each strain and culture condition was assessed in duplicate using 6-well plates and incubated for 4 hours at 37°C with 5% CO_2. Cultures were then collected,

716 centrifuged for 5 minutes at 21,130×g, and the supernatants were filter-sterilized using syringe
717 filters (0.22 µm pore size). H_2O_2 was quantified using the Amplex Red H_2O_2 assay kit
718 (Molecular Probes), according to the manufacturer's instructions. Measurements were taken
719 using an SYN H1 Hybrid Biotek reader (Agilent) or an Oroboros O2k FluoRespirometer(66).
720 **Purification of cytosolic and mitochondrial fractions and Western blotting.**
721 Calu-3 cells, infected as described, were incubated for 12 h at 37°C in 5% CO_2, with mock-
722 infected controls. At 12 h, 10 µM DCP-Rho1 (Cayman) was added for 10 min. Cells were
723 washed twice with ice-cold PBS, scraped from 6-well plates, and lysed in RIPA buffer with 1x
724 Complete Protease Inhibitor Cocktail EDTA-free (Roche) for 30 min on ice. Lysates were
725 centrifuged (13,500 × g, 20 min, 4°C), and the supernatant (cytosolic fraction) was collected.
726 Mitochondria were isolated from separate cells using the Mitochondria Isolation Kit for Cultured
727 Cells (Thermo Fisher Scientific). Protein concentrations were measured with the BCA Protein
728 Assay Kit (Thermo Fisher Scientific).
729 For Western blotting, equal protein amounts were mixed with 4× reducing sample buffer,
730 boiled (5 min, 100°C), and separated on 12% Mini-PROTEAN TGX gels (Bio-Rad) at 90 V for
731 2 h. Proteins were transferred to nitrocellulose membranes using the Trans-Blot Turbo System
732 (Bio-Rad) with 20% ethanol transfer buffer. Membranes were blocked (1 h, room temperature)
733 in TBST (0.1% Tween 20) with 5% non-fat dry milk, then incubated overnight at 4°C with
734 primary antibodies (anti-β-actin, Proteintech; anti-TRITC, Thermo Fisher Scientific; anti-
735 MTCO2, Invitrogen) in TBST with 5% milk. After three 5-min TBST washes, membranes were
736 incubated (1 h, room temperature) with StarBright Blue 520 anti-mouse or anti-rabbit
737 secondary antibodies (1:2,500, Bio-Rad) in TBST with 5% milk, followed by six 5-min TBST

washes. Blots were imaged on a ChemiDoc MP System (Bio-Rad) using Image Lab 5.0 software.

Animal information. Sprague Dawley rats were purchased from Jackson Laboratory (Maine, US) at 7 weeks of age and allowed to acclimate for at least 1 week before use. All animals were housed in the Center for Comparative Research animal facilities of the University of Mississippi Medical Center (UMMC). Animals were kept on a 12 h light/12 h dark cycle and fed a standard laboratory rodent diet (Teklad 8640). All procedures were conducted in accordance with the National Institutes of Health's Guide for the Care and Use of Laboratory Animals and approved by the UMMC Institutional Animal Care and Use Committee (Protocol #1582).

Experiments of mitochondrial respiration and mitochondrial complex activity. Measurement of mitochondrial respiration follows previously published protocols(64, 65). In brief, Spn strains were cultured in THY for 4 h 37°C with a 5% CO_2 atmosphere. Sterilized supernatants from each sample were then used to measure mitochondrial respiration driven through complex-I and II and activity through complexes I, II, III, and IV. In select experiments, catalase (to scavenge H_2O_2) or exogenous H_2O_2 (50 µM) was added to TIGR4 or TIGR4ΔspxBΔlctO supernatants to evaluate the reversibility of complex I inhibition. Complex-I driven respiration was measured through 20 mM glutamate plus 5 mM malate or 10 mM pyruvate plus 5 mM malate substrates with addition of 2 mM ADP. Complex-II driven respiration was measured through 20 mM succinate as the substrates with addition of 2 mM ADP. For fatty acid oxidation, the reaction contained 0.5 mM malate, 2 mM ATP, 1 mM NAD+, 25 µM cytochrome c, 0.1 mM coenzyme A, and either 0.5 mM oleate (long-chain fatty acid, LCFA) or 0.5 mM octanoate (medium-chain fatty acid, MCFA). All measurements were performed in an Oroboros O2K FluoRespirometer using a buffer containing 10 mM KPi, 5 mM

MgCl2, 30 mM KCl, 1 mM EDTA, and 75 mM Tris, pH 7.5. All samples were normalized to protein content as determined by BioRad DC assay and reported as nmol e-/min/mg protein. *Complex I* activity was measured as the time-dependent oxidation of NADH at 340 nm using a measured extinction coefficient of 6.22 $mM^{-1}cm^{-1}$. The reaction mixture in a regular quartz cuvette contained 10 mM KPi, 5 mM $MgCl_2$, 30 mM KCl, 1 mM EDTA, 75 mM Tris, pH 7.5, 100 µM Coenzyme Q1 (CoQ1), 5 µM antimycin A, and 5 µL heart mitochondria in a final volume of 2 mL. The reaction was initiated by adding 100 µM NADH and the fastest rates were obtained after NADH was added. *Complex II* activity was measured as the time-dependent oxidation of 2,6-dichloroindophenol sodium salt hydrate (DCPIP) at 600 nm using a measured extinction coefficient of 19.1 $mM^{-1}cm^{-1}$. The reaction mixture in a micro-cuvette contained 10 mM Kpi, 5 mM $MgCl_2$, 30 mM KCl, 1 mM EDTA, 75 mM Tris, pH 7.5, 20 mM succinate, 80 µM DCPIP, 1 mM KCN, 5 µM Antimycin A, 4 µM rotenone, and 5 µL of heart mitochondria in a final volume of 200 µL. Reactions were initiated by adding 50 µM decylubiquinone and the linear rates were obtained. *Complex III* activity was measured as the time-dependent reduction of cytochrome *c* at 550 nm using a measured extinction coefficient of 18.7 $mM^{-1}cm^{-1}$. The reaction mixture in a regular glass cuvette contained 10 mM Kpi, 5 mM $MgCl_2$, 30 mM KCl, 1 mM EDTA, 75 mM Tris, pH 7.5, 3 mM KCN, 4 µM rotenone, 60 µM cytochrome *c*, 5 µL of heart mitochondria in a final volume of 2 mL. *Complex IV* activity was measured as the time-dependent oxidation of N,N,N',N'-Tetramethyl-p-phenylenediamine dihydrochloride (TMPD) to donate electrons to cytochrome *c*. The reaction mixture in a cuvette contained 50 mM Tris, 8 mM KCl, 1 mM EDTA, 16 µg/µL catalase, pH 7.4, 3 mM ascorbate, 0.3 mM TMPD, and 25 µM cytochrome c. Reactions were initiated with 100 µM reduced decylubiquinone. The rate was linear for 1-2 min. *Aconitase* activity was measured as the time-dependent formation of cis-aconitate at 240

nm using a measured extinction coefficient of 2.2 $mM^{-1}cm^{-1}$ (67). The reaction mixture in a quartz cuvette containing 50 mM Tris–HCl (pH 7.4) containing 0.6 mM MnCl2, 30 mM citrate, and 0.2% peroxide-free Triton-X 100. For each enzyme, the inhibited non-enzymatic background rates were subtracted from the enzymatic rates. *Glutamate dehydrogenase* and *α-ketoglutarate dehydrogenase* were measured using the kits from Sigma (MAK099 and MAK189) following the provided protocols.

Flow cytometry analysis using caspase-3/7 reagent and JC-1 assay. To assess mitochondrial membrane potential and apoptosis in human alveolar A549 cells infected with Spn, the MitoProbe JC-1 assay kit (Invitrogen) and the CellEvent Caspase-3/7 Green Detection Reagent (ThermoFisher) were employed. A549 cells grown in a 6-well plate were washed and treated with infection media as described above. Cells were then infected with Spn and incubated for 10 h. After incubation, cells were lifted from the wells using 0.25% Trypsin-EDTA, counted, and ~1×10^6 cells were used for JC-1 staining following the manufacturer's protocol. For caspase-3/7 detection, cells were incubated with the CellEvent Caspase-3/7 Green Detection Reagent (2 µM final concentration) for 30 minutes at 37°C prior to analysis, following the manufacturer's instructions. As a control, uninfected cells were treated with 125 µM Carbonyl cyanide m-chlorophenyl hydrazone (CCCP) for 10 minutes or 2 mM H_2O_2 for 1 h to induce mitochondrial depolarization or oxidative stress, respectively. In addition, staurosporine (Sigma, 1 µM and 10 µM, 4 hours) was used as a positive control for caspase-3/7 activation. Subsequently, cells were stained with 1 µM SYTOX Blue Dead Cell Stain (Invitrogen) for dead cells. Flow cytometry was performed on a NovoCyte (Agilent). JC-1 was excited with a 488 nm laser, and the emission was collected in the PE-Texas Red (red, 615/20) and FITC (green, 530/30) channels, to assess mitochondrial membrane potential.

807 Caspase-3/7 activation was detected in the FITC channel (530/30 nm filter) following excitation
808 at 488 nm. SYTOX Blue Dead Cell Stain was excited by the violet 405 nm laser and detected
809 in the 530/30 nm channel. Fluorescence compensation, including correction for JC-1 spectral
810 overlap between FITC and Texas Red channels, was performed using FMO and single-color
811 controls. Data from 50,000 events per sample were acquired and analyzed using NovoExpress
812 software (Agilent).

813 **TUNEL assay.** To identify late-stage apoptosis in Spn-infected human alveolar A549 cells, the
814 Click-iT Plus TUNEL assay kit (Invitrogen) was utilized. A549 cells were seeded in a 6-well
815 plate with glass coverslips and used after ~7-10 days post-seeding. Before infection, A549
816 cells were washed and treated with infection media as described above. Cells were then
817 infected with the indicated Spn strain and incubated for 8 h. As a control, some cells were
818 treated with 2 mM H_2O_2 every 2 h for 8 h. After incubation, cells were stained following the
819 manufacturer's protocol. Following staining, cells were washed, coverslips were removed, and
820 the cells were allowed to dry before being mounted and stained for DNA using ProLong Gold
821 Antifade Mountant containing DAPI. Slides were then imaged using a Nikon A1R HD25 laser
822 scanning confocal upright microscope. Confocal images were analyzed using Imaris x64
823 software version 10.1.0.

824 **Activity of glutamate dehydrogenase in bronchial Calu-3 cells infected with**
825 **pneumococcal strains**. Calu-3 cells grown in 100 mm tissue culture-treated dishes (Fisher)
826 were washed three times with sterile PBS to remove antibiotics and then added with 10 ml of
827 infection medium, consisting of EMEM supplemented with 1% HEPES buffer and 5% fetal
828 bovine serum (FBS). Cells were either mock-infected or infected with TIGR4 or
829 TIGR4Δ*spxB*Δ*lctO* and incubated for 8 h at 37°C in a 5% CO_2 atmosphere. The supernatant,

containing the planktonic bacterial fraction, was collected for HPLC studies, as detailed below. Infected cells were washed once with PBS and harvested using a cell scraper in 1 ml of cold sterile PBS. The cells were centrifuged at 300 × g for 5 minutes, and the resulting pellet was resuspended in 200 µl of PBS. The cells were then lysed using a Dounce homogenizer, and the lysate volume was adjusted to 600 µL with sterile PBS. The lysate was centrifuged at 10,000 × g for 15 minutes at 4°C, and the soluble fraction was used to assess the enzymatic activity of glutamate dehydrogenase (GDH) and for HPLC analysis. Assays were performed in technical triplicates with two biological replicates.

Glutamate dehydrogenase activity and metabolite quantification in Spn-infected human respiratory cells. Human bronchial Calu-3 cells were cultured for 10 days in 55 cm^2 Petri dishes in Eagle's Minimum Essential Medium (EMEM) supplemented with 1% HEPES buffer and 5% fetal bovine serum (FBS). Cells were washed three times with sterile phosphate-buffered saline (PBS) to remove antibiotics and overlaid with 10 ml of infection medium (EMEM with 1% HEPES and 5% FBS). Cells were infected with Spn strains and incubated at 37°C for 8 h. Mock-infected cells served as controls. For secreted metabolite analysis, 1 ml of infection medium was centrifuged at 10,000 × g for 5 min to remove planktonic bacteria, and the supernatant was collected. Cells were washed once with PBS, scraped in 1 ml PBS, and centrifuged at 300 × g for 5 min. For glutamate dehydrogenase (GDH) activity, the cell pellet was resuspended in 200 µl PBS, homogenized using a Dounce homogenizer, diluted with 400 µl PBS, and centrifuged at 10,000 × g for 15 min. The resulting supernatant (cell extract) was used for GDH activity assays and intracellular metabolite quantification. GDH activity was measured using a non-radioactive colorimetric assay (MAK499-1KT, Sigma-Aldrich, St. Louis, MO) according to the manufacturer's instructions. For metabolite quantification, lactate,

acetate, and citrate levels in cell-free supernatants (extracellular) and cell extracts (intracellular) were analyzed by high-performance liquid chromatography (HPLC) using a Thermo Dionex Ultimate 3000 UHPLC System equipped with an Aminex HPX-87H column (Bio-Rad, Hercules, CA) maintained at 25°C. An isocratic elution was performed with 5 mM H_2SO_4 at a flow rate of 0.6 mL/min, and metabolites were detected at 208 nm. Samples were prepared by mixing 100 µl of supernatant or cell extract with 100 µl of 95% ethanol, incubating at –80°C for 15 min to precipitate proteins, and centrifuging at 20,000 × g for 15 min. A 20 µl aliquot of the resulting supernatant was injected for analysis. All assays were performed with two technical triplicates and three biological replicates. Statistical analyses are described in the relevant figure legends.

Statistical analysis. We performed one-way analysis of variance (ANOVA) followed by Dunnett's multiple-comparison test when two or more groups were involved. All analysis was performed using GraphPad Prism software (version 10.2.1).

ACKNOWLEDGEMENTS

This study was supported in part by grants from the National Institutes of Health (NIH), including R21AI144571, R01AI175461 (to J.E.V.) and R01GM142113 and RR17767 (to K.W.). Confocal microscopy and mitochondrial respiration studies (K.E.) were supported by the National Institute of General Medical Sciences (NIGMS) under Award Number P20GM121334. J.E.V. is also supported by NIGMS through the Molecular Center of Health and Disease (P20GM144041). RNA-seq data analysis was performed at the UMMC Molecular and Genomics Facility, supported by funds from NIGMS (P20GM144041), Mississippi INBRE (P20GM103476), the Obesity, Cardiorenal, and Metabolic Diseases COBRE (P30GM149404),

and the Mississippi Center of Perinatal Research (P20GM121334). The content is solely the responsibility of the authors and does not necessarily represent the official views of the NIH or the U.S. Department of State. The authors thank Dr. David Brown (UMMC) for his assistance with confocal microscopy.

DISCLOSURE STATEMENTS

The authors report that there are no competing interests to declare.

References

1. Kadioglu A, Weiser JN, Paton JC, Andrew PW. 2008. The role of Streptococcus pneumoniae virulence factors in host respiratory colonization and disease. Nat Rev Microbiol 6:288–301.
2. van der Poll T, Opal SM. 2009. Pathogenesis, treatment, and prevention of pneumococcal pneumonia. Lancet 374:1543–56.
3. Feldman C, Anderson R, Cockeran R, Mitchell T, Cole P, Wilson R. 2002. The effects of pneumolysin and hydrogen peroxide, alone and in combination, on human ciliated epithelium in vitro. Respir Med 96:580–5.
4. Rai P, Parrish M, Tay IJ, Li N, Ackerman S, He F, Kwang J, Chow VT, Engelward BP. 2015. Streptococcus pneumoniae secretes hydrogen peroxide leading to DNA damage and apoptosis in lung cells. Proc Natl Acad Sci U S A 112:E3421–30.
5. Scasny A, Alibayov B, Khan F, Rao SJ, Murin L, Jop Vidal AG, Smith P, Li W, Edwards K, Warncke K, Vidal JE. 2023. Oxidation of hemoproteins by Streptococcus pneumoniae collapses the cell cytoskeleton and disrupts mitochondrial respiration

leading to the cytotoxicity of human lung cells. Microbiol Spectr doi:10.1128/spectrum.02912-23:e0291223.

6. Bogaert D, De Groot R, Hermans PW. 2004. Streptococcus pneumoniae colonisation: the key to pneumococcal disease. Lancet Infect Dis 4:144–54.

7. Lisher JP, Tsui HT, Ramos-Montanez S, Hentchel KL, Martin JE, Trinidad JC, Winkler ME, Giedroc DP. 2017. Biological and Chemical Adaptation to Endogenous Hydrogen Peroxide Production in Streptococcus pneumoniae D39. mSphere 2.

8. Pericone CD, Park S, Imlay JA, Weiser JN. 2003. Factors contributing to hydrogen peroxide resistance in Streptococcus pneumoniae include pyruvate oxidase (SpxB) and avoidance of the toxic effects of the fenton reaction. J Bacteriol 185:6815–25.

9. Wu X, Gordon O, Jiang W, Antezana BS, Angulo-Zamudio UA, Del Rio C, Moller A, Brissac T, Tierney ARP, Warncke K, Orihuela CJ, Read TD, Vidal JE. 2019. Interaction between Streptococcus pneumoniae and Staphylococcus aureus Generates (.)OH Radicals That Rapidly Kill Staphylococcus aureus Strains. J Bacteriol 201.

10. Mraheil MA, Toque HA, La Pietra L, Hamacher J, Phanthok T, Verin A, Gonzales J, Su Y, Fulton D, Eaton DC, Chakraborty T, Lucas R. 2021. Dual Role of Hydrogen Peroxide as an Oxidant in Pneumococcal Pneumonia. Antioxid Redox Signal 34:962–978.

11. Shenoy AT, Brissac T, Gilley RP, Kumar N, Wang Y, Gonzalez-Juarbe N, Hinkle WS, Daugherty SC, Shetty AC, Ott S, Tallon LJ, Deshane J, Tettelin H, Orihuela CJ. 2017. Streptococcus pneumoniae in the heart subvert the host response through biofilm-mediated resident macrophage killing. PLoS Pathog 13:e1006582.

12. Brissac T, Shenoy AT, Patterson LA, Orihuela CJ. 2017. Cell invasion and pyruvate oxidase derived H2O2 are critical for Streptococcus pneumoniae mediated cardiomyocyte killing. Infect Immun doi:10.1128/IAI.00569-17.

13. Ramos-Montanez S, Tsui HC, Wayne KJ, Morris JL, Peters LE, Zhang F, Kazmierczak KM, Sham LT, Winkler ME. 2008. Polymorphism and regulation of the spxB (pyruvate oxidase) virulence factor gene by a CBS-HotDog domain protein (SpxR) in serotype 2 Streptococcus pneumoniae. Mol Microbiol 67:729–46.

14. Echlin H, Frank MW, Iverson A, Chang TC, Johnson MD, Rock CO, Rosch JW. 2016. Pyruvate Oxidase as a Critical Link between Metabolism and Capsule Biosynthesis in Streptococcus pneumoniae. PLoS Pathog 12:e1005951.

15. Spellerberg B, Cundell DR, Sandros J, Pearce BJ, Idanpaan-Heikkila I, Rosenow C, Masure HR. 1996. Pyruvate oxidase, as a determinant of virulence in Streptococcus pneumoniae. Mol Microbiol 19:803–13.

16. Rubins JB, Duane PG, Clawson D, Charboneau D, Young J, Niewoehner DE. 1993. Toxicity of pneumolysin to pulmonary alveolar epithelial cells. Infect Immun 61:1352–8.

17. Scasny A, Alibayov B, Khan F, Rao SJ, Murin L, Jop Vidal AG, Smith P, Wei L, Edwards K, Warncke K, Vidal JE. 2023. Oxidation of hemoproteins by Streptococcus pneumoniae collapses the cell cytoskeleton and disrupts mitochondrial respiration leading to cytotoxicity of human lung cells. bioRxiv doi:10.1101/2023.06.07.544089.

18. Gao Y, Xu W, Dou X, Wang H, Zhang X, Yang S, Liao H, Hu X, Wang H. 2019. Mitochondrial DNA Leakage Caused by Streptococcus pneumoniae Hydrogen Peroxide Promotes Type I IFN Expression in Lung Cells. Front Microbiol 10:630.

19. Plataki M, Cho SJ, Harris RM, Huang HR, Yun HS, Schiffer KT, Stout-Delgado HW. 2019. Mitochondrial Dysfunction in Aged Macrophages and Lung during Primary Streptococcus pneumoniae Infection is Improved with Pirfenidone. Sci Rep 9:971.

20. Chun YY, Tan KS, Yu L, Pang M, Wong MHM, Nakamoto R, Chua WZ, Huee-Ping Wong A, Lew ZZR, Ong HH, Chow VT, Tran T, Yun Wang D, Sham LT. 2023. Influence of glycan structure on the colonization of Streptococcus pneumoniae on human respiratory epithelial cells. Proc Natl Acad Sci U S A 120:e2213584120.

21. Surabhi S, Jachmann LH, Shumba P, Burchhardt G, Hammerschmidt S, Siemens N. 2022. Hydrogen Peroxide Is Crucial for NLRP3 Inflammasome-Mediated IL-1beta Production and Cell Death in Pneumococcal Infections of Bronchial Epithelial Cells. J Innate Immun 14:192–206.

22. Brissac T, Shenoy AT, Patterson LA, Orihuela CJ. 2018. Cell Invasion and Pyruvate Oxidase-Derived H(2)O(2) Are Critical for Streptococcus pneumoniae-Mediated Cardiomyocyte Killing. Infect Immun 86.

23. Alibayov B, Scasny A, Vidal AGJ, Murin L, Wong S, Edwards KS, Eichembaun Z, Punshon T, Jackson BP, Hopp MT, McDaniel LS, Akerley BJ, Imhof D, Vidal JE. 2023. Oxidation of hemoglobin in the lung parenchyma facilitates the differentiation of pneumococci into encapsulated bacteria. bioRxiv doi:10.1101/2023.11.14.567109.

24. Landino LM, Hagedorn TD, Kim SB, Hogan KM. 2011. Inhibition of tubulin polymerization by hypochlorous acid and chloramines. Free Radic Biol Med 50:1000–8.

25. Clark HM, Hagedorn TD, Landino LM. 2014. Hypothiocyanous acid oxidation of tubulin cysteines inhibits microtubule polymerization. Arch Biochem Biophys 541:67–73.

26. Goldblum RR, McClellan M, White K, Gonzalez SJ, Thompson BR, Vang HX, Cohen H, Higgins L, Markowski TW, Yang TY, Metzger JM, Gardner MK. 2021. Oxidative stress pathogenically remodels the cardiac myocyte cytoskeleton via structural alterations to the microtubule lattice. Dev Cell 56:2252–2266 e6.

27. Vallelian F, Pimenova T, Pereira CP, Abraham B, Mikolajczyk MG, Schoedon G, Zenobi R, Alayash AI, Buehler PW, Schaer DJ. 2008. The reaction of hydrogen peroxide with hemoglobin induces extensive alpha-globin crosslinking and impairs the interaction of hemoglobin with endogenous scavenger pathways. Free Radic Biol Med 45:1150–8.

28. Jia Y, Buehler PW, Boykins RA, Venable RM, Alayash AI. 2007. Structural basis of peroxide-mediated changes in human hemoglobin: a novel oxidative pathway. J Biol Chem 282:4894–4907.

29. Osellame LD, Blacker TS, Duchen MR. 2012. Cellular and molecular mechanisms of mitochondrial function. Best Pract Res Clin Endocrinol Metab 26:711–23.

30. Akram M. 2014. Citric acid cycle and role of its intermediates in metabolism. Cell Biochem Biophys 68:475–8.

31. Kim HJ, Khalimonchuk O, Smith PM, Winge DR. 2012. Structure, function, and assembly of heme centers in mitochondrial respiratory complexes. Biochim Biophys Acta 1823:1604–16.

32. Schumacker PT, Gillespie MN, Nakahira K, Choi AM, Crouser ED, Piantadosi CA, Bhattacharya J. 2014. Mitochondria in lung biology and pathology: more than just a powerhouse. Am J Physiol Lung Cell Mol Physiol 306:L962–74.

33. Sharma LK, Lu J, Bai Y. 2009. Mitochondrial respiratory complex I: structure, function and implication in human diseases. Curr Med Chem 16:1266–77.

34. Alibayov B, Scasny A, Khan F, Creel A, Smith P, Vidal AGJ, Fitisemanu FM, Padilla-Benavides T, Weiser JN, Vidal JE. 2022. Oxidative Reactions Catalyzed by Hydrogen Peroxide Produced by Streptococcus pneumoniae and Other Streptococci Cause the Release and Degradation of Heme from Hemoglobin. Infect Immun 90:e0047122.

35. Lanie JA, Ng WL, Kazmierczak KM, Andrzejewski TM, Davidsen TM, Wayne KJ, Tettelin H, Glass JI, Winkler ME. 2007. Genome sequence of Avery's virulent serotype 2 strain D39 of Streptococcus pneumoniae and comparison with that of unencapsulated laboratory strain R6. J Bacteriol 189:38–51.

36. Tettelin H, Nelson KE, Paulsen IT, Eisen JA, Read TD, Peterson S, Heidelberg J, DeBoy RT, Haft DH, Dodson RJ, Durkin AS, Gwinn M, Kolonay JF, Nelson WC, Peterson JD, Umayam LA, White O, Salzberg SL, Lewis MR, Radune D, Holtzapple E, Khouri H, Wolf AM, Utterback TR, Hansen CL, McDonald LA, Feldblyum TV, Angiuoli S, Dickinson T, Hickey EK, Holt IE, Loftus BJ, Yang F, Smith HO, Venter JC, Dougherty BA, Morrison DA, Hollingshead SK, Fraser CM. 2001. Complete genome sequence of a virulent isolate of Streptococcus pneumoniae. Science 293:498–506.

37. McDevitt E, Khan F, Scasny A, Thompson CD, Eichenbaum Z, McDaniel LS, Vidal JE. 2020. Hydrogen Peroxide Production by Streptococcus pneumoniae Results in Alpha-hemolysis by Oxidation of Oxy-hemoglobin to Met-hemoglobin. mSphere 5.

38. Nagababu E, Rifkind JM. 2000. Heme degradation during autoxidation of oxyhemoglobin. Biochem Biophys Res Commun 273:839–45.

39. Hulko M, Hospach I, Krasteva N, Nelles G. 2011. Cytochrome c biosensor--a model for gas sensing. Sensors (Basel) 11:5968–80.

40. Koch H-G, Schneider, Dirk. 2007. Folding, Assembly, and Stability of Transmembrane Cytochromes. Current Chemical Biology 1:59–74.

41. Imlay JA, Chin SM, Linn S. 1988. Toxic DNA damage by hydrogen peroxide through the Fenton reaction in vivo and in vitro. Science 240:640–2.

42. Winterbourn CC. 1995. Toxicity of iron and hydrogen peroxide: the Fenton reaction. Toxicol Lett 82-83:969–74.

43. Chen YR, Chen CL, Chen W, Zweier JL, Augusto O, Radi R, Mason RP. 2004. Formation of protein tyrosine ortho-semiquinone radical and nitrotyrosine from cytochrome c-derived tyrosyl radical. J Biol Chem 279:18054–62.

44. Lawrence A, Jones CM, Wardman P, Burkitt MJ. 2003. Evidence for the role of a peroxidase compound I-type intermediate in the oxidation of glutathione, NADH, ascorbate, and dichlorofluorescin by cytochrome c/H2O2. Implications for oxidative stress during apoptosis. J Biol Chem 278:29410–9.

45. Alibayov B, Jop Vidal AG, Murin L, Scasny A, Takeshita K, Beeton K, Edwards KS, Punshon T, Jackson BP, McDaniel LS, Vidal JE. 2025. Heme-mediated selection of encapsulated Streptococcus pneumoniae in the lungs by oxidative stress. Emerg Microbes Infect 14:2532685.

46. Scasny A, Alibayov B, Khan F, Rao SJ, Murin L, Jop Vidal AG, Smith P, Li W, Edwards K, Warncke K, Vidal JE. 2024. Oxidation of hemoproteins by Streptococcus pneumoniae collapses the cell cytoskeleton and disrupts mitochondrial respiration leading to the cytotoxicity of human lung cells. Microbiol Spectr 12:e0291223.

47. Youle RJ, van der Bliek AM. 2012. Mitochondrial fission, fusion, and stress. Science 337:1062–5.

48. Gnaiger E. Mitochondrial pathways and respiratory control: An Introduction to OXPHOS Analysis. 5th ed, p. *In* (ed),

49. Surabhi S, Jachmann LH, Lalk M, Hammerschmidt S, Methling K, Siemens N. 2021. Bronchial Epithelial Cells Accumulate Citrate Intracellularly in Response to Pneumococcal Hydrogen Peroxide. ACS Infect Dis 7:2971–2978.

50. Poole LB, Klomsiri C, Knaggs SA, Furdui CM, Nelson KJ, Thomas MJ, Fetrow JS, Daniel LW, King SB. 2007. Fluorescent and affinity-based tools to detect cysteine sulfenic acid formation in proteins. Bioconjug Chem 18:2004–17.

51. Zhu Y, Chidekel A, Shaffer TH. 2010. Cultured human airway epithelial cells (calu-3): a model of human respiratory function, structure, and inflammatory responses. Crit Care Res Pract 2010.

52. Klabunde B, Wesener A, Bertrams W, Beinborn I, Paczia N, Surmann K, Blankenburg S, Wilhelm J, Serrania J, Knoops K, Elsayed EM, Laakmann K, Jung AL, Kirschbaum A, Hammerschmidt S, Alshaar B, Gisch N, Abu Mraheil M, Becker A, Volker U, Vollmeister E, Benedikter BJ, Schmeck B. 2023. NAD(+) metabolism is a key modulator of bacterial respiratory epithelial infections. Nat Commun 14:5818.

53. Dabral S, Muecke C, Valasarajan C, Schmoranzer M, Wietelmann A, Semenza GL, Meister M, Muley T, Seeger-Nukpezah T, Samakovlis C, Weissmann N, Grimminger F, Seeger W, Savai R, Pullamsetti SS. 2019. A RASSF1A-HIF1alpha loop drives Warburg effect in cancer and pulmonary hypertension. Nat Commun 10:2130.

54. Lim S, Liu H, Madeira da Silva L, Arora R, Liu Z, Phillips JB, Schmitt DC, Vu T, McClellan S, Lin Y, Lin W, Piazza GA, Fodstad O, Tan M. 2016. Immunoregulatory

Protein B7-H3 Reprograms Glucose Metabolism in Cancer Cells by ROS-Mediated Stabilization of HIF1alpha. Cancer Res 76:2231–42.

55. Zorova LD, Popkov VA, Plotnikov EY, Silachev DN, Pevzner IB, Jankauskas SS, Babenko VA, Zorov SD, Balakireva AV, Juhaszova M, Sollott SJ, Zorov DB. 2018. Mitochondrial membrane potential. Anal Biochem 552:50–59.

56. Kress TR, Sabo A, Amati B. 2015. MYC: connecting selective transcriptional control to global RNA production. Nat Rev Cancer 15:593–607.

57. Titov DV, Cracan V, Goodman RP, Peng J, Grabarek Z, Mootha VK. 2016. Complementation of mitochondrial electron transport chain by manipulation of the NAD+/NADH ratio. Science 352:231–5.

58. Weiser JN, Ferreira DM, Paton JC. 2018. Streptococcus pneumoniae: transmission, colonization and invasion. Nat Rev Microbiol 16:355–367.

59. DeBerardinis RJ, Chandel NS. 2020. We need to talk about the Warburg effect. Nat Metab 2:127–129.

60. Mado K, Chekulayev V, Shevchuk I, Puurand M, Tepp K, Kaambre T. 2019. On the role of tubulin, plectin, desmin, and vimentin in the regulation of mitochondrial energy fluxes in muscle cells. Am J Physiol Cell Physiol 316:C657–C667.

61. Guzun R, Karu-Varikmaa M, Gonzalez-Granillo M, Kuznetsov AV, Michel L, Cottet-Rousselle C, Saaremae M, Kaambre T, Metsis M, Grimm M, Auffray C, Saks V. 2011. Mitochondria-cytoskeleton interaction: distribution of beta-tubulins in cardiomyocytes and HL-1 cells. Biochim Biophys Acta 1807:458–69.

62. Nulton-Persson AC, Szweda LI. 2001. Modulation of mitochondrial function by hydrogen peroxide. J Biol Chem 276:23357–61.

63. O'Brien KL, Bronsdon MA, Dagan R, Yagupsky P, Janco J, Elliott J, Whitney CG, Yang YH, Robinson LG, Schwartz B, Carlone GM. 2001. Evaluation of a medium (STGG) for transport and optimal recovery of Streptococcus pneumoniae from nasopharyngeal secretions collected during field studies. J Clin Microbiol 39:1021–4.

64. Edwards KS, Ashraf S, Lomax TM, Wiseman JM, Hall ME, Gava FN, Hall JE, Hosler JP, Harmancey R. 2018. Uncoupling protein 3 deficiency impairs myocardial fatty acid oxidation and contractile recovery following ischemia/reperfusion. Basic Res Cardiol 113:47.

65. Shirey K, Stover KR, Cleary J, Hoang N, Hosler J. 2016. Membrane-Anchored Cyclic Peptides as Effectors of Mitochondrial Oxidative Phosphorylation. Biochemistry 55:2100–11.

66. Makrecka-Kuka M, Krumschnabel G, Gnaiger E. 2015. High-Resolution Respirometry for Simultaneous Measurement of Oxygen and Hydrogen Peroxide Fluxes in Permeabilized Cells, Tissue Homogenate and Isolated Mitochondria. Biomolecules 5:1319–38.

67. Tretter L, Ambrus A. 2014. Measurement of ROS homeostasis in isolated mitochondria. Methods Enzymol 547:199–223.

68. Han S, Lee M, Shin Y, Giovanni R, Chakrabarty RP, Herrerias MM, Dada LA, Flozak AS, Reyfman PA, Khuder B, Reczek CR, Gao L, Lopez-Barneo J, Gottardi CJ, Budinger GRS, Chandel NS. 2023. Mitochondrial integrated stress response controls lung epithelial cell fate. Nature 620:890–897.

69. Junges R, Maienschein-Cline M, Morrison DA, Petersen FC. 2019. Complete Genome Sequence of Streptococcus pneumoniae Serotype 19F Strain EF3030. Microbiol Resour Announc 8.

Figure legends

Figure 1. Spn-H_2O_2 induces cytochrome c oxidation and tyrosyl radical formation. (A-F) Spn strains were incubated in THY-Cyt*c* medium at 37°C with 5% CO_2. At the indicated time (A, C) or 6 h post-inoculation (B, D, E, F), supernatants were analyzed by spectroscopy. Controls included mock-infected medium (Cyt*c*), or TIGR4 and EF3030 supplemented with 500 U catalase. Panels (A, C) show 405 nm absorbance, (B, D) show Soret peak absorbance, and panels (E, F) display α and β peak absorbance. Data represent means ± standard error (SE) from N=3 independent experiments, each with two technical duplicates. Statistical significance was assessed using one-way ANOVA with Dunnett's post hoc test (A, C) or Student's t-test (B, D). Significance levels: NS, not significant; *$p < 0.05$; **$p < 0.001$; ***$p < 0.0005$; ****$p < 0.0001$. (G) For spin-trapping, supernatants from Spn strains cultured for 4 h in THY medium were used. Cytochrome c (Cytc, 56 µM) and DEPMPO (30 mM) were added to supernatants to a final volume of 40 µL. Spectra (-Cyt*c*, black; +Cyt*c*, red) represent an average of 20 scans, corrected for buffer baseline. Uninfected THY medium served as a control (ctrl). Spn-H_2O_2-free samples (+Cat) were prepared by pretreating supernatants with catalase for 1 min.

Figure 2. Spn-H_2O_2 modifies mitochondrial morphology, induces aggregation, and promotes mislocalization. Human alveolar A549 cells were either mock-infected or infected with Spn strains and incubated for 8 h at 37°C with 5% CO_2. Infected cells were stained for mitochondria (green), DNA (blue), and actin (red), imaged via confocal microscopy, and analyzed using Imaris software. Panels (A and B) display XY optical-middle sections (0.5 µm)

from z-stacks. Panel (B) additionally includes XY, XZ (bottom), and YZ (side) optical sections. Three-dimensional reconstructions were generated from z-stacks, with panel (C) presenting simultaneous XY and XZ optical sections. Arrows in panels (B, C) indicate aggregated mitochondria. Confocal microscopy images are representative of at least three independent experiments. (D-G) Imaris software was employed to generate masks from the mitochondrial channel, enabling the assessment of subcellular localization (apical, middle, or basal) and quantification of mitochondrial area (µm²). Panel (D) depicts cells infected with strain EF3030, with the top panel showing all z-stacks, highlighting predominant apical mislocalization of mitochondria, and the bottom panel a middle optical section. Panel (E) presents three-dimensional images across all conditions as in (D), while panel (F and G) quantifies mitochondrial area under each infection condition. Data are expressed as mean ± SEM from confocal micrographs of three independent experiments. Statistical significance was assessed using one-way ANOVA with Dunnett's post hoc test, and **** indicating $p < 0.0001$.

Figure 3. Selective inhibition of complex I-driven respiration by Spn-H_2O_2. (A) H_2O_2 concentrations in supernatants from Spn cultured in THY medium (37°C, 4 h) were quantified using Amplex Red assay (LOD<0.56 µM). Data represent mean ± SEM; unpaired Student's t-test, ****$p < 0.0001$. (B) Schematic of the mitochondrial ETC in lung epithelial cells(68). (C-E) Heart mitochondria were treated with filter-sterilized Spn culture supernatants from Spn strains collected after 4 h of growth. (C, E, G-J) Complex I-driven respiration (CIDR) and (D) Complex II-driven respiration (CIIDR) were measured via Oroboros O2K FluoRespirometry. (F) Residual Complex I and II enzymatic activities relative to mock-treated controls. (G) CIDR in mitochondria treated with TIGR4 supernatants with or without catalase. (H-I) CIDR in mitochondria treated with TIGR4 Δ*spxB*Δ*lctO*, or EF3030 Δ*spxB*Δ*lctO* supernatants with or

without exogenous H_2O_2 (50 µM), compared to mock-treated controls. (J) CIDR inhibition by exogenous H_2O_2 (50 µM). (K) Complex I activity in mitochondria treated with Spn supernatants (~50 µM H_2O_2) or mock-treated controls, measured as NADH oxidation rate normalized to protein content. Data represent mean ± SEM; (F, H-J) unpaired Student's t-test, *$p < 0.05$; (C-E, G, K) one-way ANOVA with Dunnett's post hoc test, ns, not significant; *$p < 0.05$; **$p < 0.005$; ****$p < 0.0001$.

Figure 4. *Streptococcus pneumoniae*-derived H_2O_2 inhibits TCA cycle enzymes and mitochondrial respiration. (A) Diagram of the canonical tricarboxylic acid (TCA) cycle, highlighting enzymes and electron donors (NADH, $FADH_2$). ETF, electron-transferring flavoprotein complex; α-KG, alpha-ketoglutarate. (B, C) Heart mitochondria were mock-treated or treated with filter-sterilized Spn culture supernatants (~50 µM H_2O_2, collected after 4 h growth). (B) Complex I-driven respiration (CIDR) and Complex II-driven respiration (CIIDR) were measured using Oroboros O2K FluoRespirometry with substrates: (CIDR) 10 mM pyruvate, 5 mM malate, 2 mM ADP, or 20 mM glutamate, 5 mM malate, 2 mM ADP; (CIIDR) 20 mM succinate, 2 mM ADP. (C) CIDR was measured with fatty acid substrates oleate and octanoate. (D–F) Enzymatic activities of aconitase, glutamate dehydrogenase (GDH), and α-ketoglutarate dehydrogenase were measured in heart mitochondria mock-treated or treated with Spn supernatants (~50 µM H_2O_2), as described in Materials and Methods. (G) GDH activity was assessed in Calu-3 lung epithelial cells infected with Spn strains. (H, I) RNA-seq analysis of human bronchial Calu-3 cells mock-infected or infected with Spn strains. Heatmaps depict expression of (H) mitochondria-related or (I) oxidative stress-related genes; NS, not significant. (J) Diagram of cysteine oxidation experimental design. (K) Chemical reaction illustrating H_2O_2-mediated cysteine oxidation. (L) Cytosolic fraction appearance post-DCP-

Rho1 incubation. (M, N) Western blot analysis of (M) cytosolic and (N) mitochondrial fractions using anti-TRITC antibodies (anti-RhoI), with β-actin and cytochrome c oxidase subunit II as respective loading controls. (B–G) Data represent mean ± SEM; one-way ANOVA with Dunnett's post hoc test, ns, not significant; *p < 0.05; **p < 0.005; ***p < 0.0005; ****p < 0.0001.

Figure 5. Spn-H_2O_2 drives Warburg-like metabolic reprogramming in lung epithelial cells. (A–C, E–G) Human bronchial Calu-3 cells were mock-infected, infected with Spn strains, or incubated with Spn cultured in cell culture medium for 8 h. Culture supernatants (extracellular) or cell pellets (intracellular) were harvested to quantify levels of (A, B) citrate, (C) glucose, (E) acetate, and (F, G) lactate, as described in Materials and Methods. Data represent mean ± SEM; one-way ANOVA with Dunnett's post hoc test (versus mock-infected cells) or unpaired Student's t-test (versus TIGR4 strain); ns, not significant; *p < 0.05; **p < 0.005; ***p < 0.0005; ****p < 0.0001. (D) Diagram of pyruvate node reactions under aerobic conditions, incorporating oxaloacetate and citrate. Enzymes are highlighted in gray. (H) RNA-seq analysis of Calu-3 cells or (I) BEAS 2B mock-infected or infected with Spn strains. Heatmap depicts expression of glycolysis-related genes; NS, not significant. (K) Schematic of the canonical glycolysis pathway, highlighting genes encoding enzymes upregulated in RNA-seq analysis.

Figure 6. *Streptococcus pneumoniae*-derived H_2O_2 does not significantly alter mitochondrial membrane potential in lung epithelial cells. (A–H) Human alveolar A549 cells were mock-treated, treated with CCCP, H_2O_2, EF3030, EF3030Δ*spxB*Δ*lctO* or EF3030 and CCCP for 10 h. Cells were stained with JC-1 dye for flow cytometric analysis and counterstained with SYTOX Blue to exclude dead cells. (A–F) Scatter plots showing JC-1 fluorescence (PE-TexasRed/FITC) for each condition, with gating to identify live cells. (G and I)

Quantification of change in mitochondrial membrane potential (Δψm) or (H and J) percent of live cells expressed as mean ± SEM from three independent experiment; one-way ANOVA with Dunnett's post hoc test; ns, not significant; *p < 0.05; **p < 0.01; ****p < 0.0001.

Figure 7. Limited contribution of Spn-H_2O_2 to apoptosis in lung epithelial cells. (A) Human alveolar A549 cells were mock-infected, treated with DNaseI (1U), treated with H_2O_2 (2 mM) added every 2 h, or infected with TIGR4, TIGR4Δ*spxB*Δ*lctO*, EF3030, or EF3030Δ*spxB*Δ*lctO* for 10 h. Cells were stained with the Click-iT Plus TUNEL assay kit, and mounted on slides with DAPI-containing resin and analyzed by confocal microscopy using the Imaris software. (B) Fluorescence intensity (FITC/GFP) from each condition, reported as arbitrary units (AU), quantifying TUNEL staining. (C) A549 cells were mock-infected or infected with EF3030, EF3030Δ*spxB*Δ*lctO* for 10 h or treated with staurosporine (10 µM, 4 h), then stained with Cell Event Caspase-3/7 Green Detection Reagent (2 µM) and SYTOX Blue Dead Cell Stain (1 µM) prior to flow cytometric analysis. Representative bivariate density plots show the percentages of single A549 cells within the P3 gate: non-apoptotic SYTOX blue–positive cells (Q4-1), SYTOX blue–negative non-apoptotic cells (Q4-3), and caspase-3/7–positive, SYTOX blue–negative cells (Q4-4) for each condition. (D) Percentage of SYTOX Blue-negative live cells, and among those, the proportion of caspase-3/7 positive cells. (B, D) Data represent mean ± SEM from two independent experiments with four (B) or two (D) internal replicates each; one-way ANOVA with Dunnett's post hoc test; ns, not significant; *p < 0.05; **p < 0.01; ****p < 0.0001. (E-F) Cells treated with staurosporine (10 µM) for 7 hours or infected with EF3030 for 10 hours were stained with WGA, caspase-3/7 reagent, and DAPI as indicated. Z-stacks were acquired in real-time using confocal microscopy at the specified time points. Displayed are the middle sections of 3D images from z-stacks (left panels) and the

corresponding XY, XZ, and YZ optical sections (right panels). (D, E) RNA-seq analysis of Calu-3 (D) or BEAS-2B (E) cells mock-infected or infected for 9 or 16 h with Spn strains. Heatmaps depict expression of mitochondria-related and apoptosis-related genes

Table 1. Strains utilized in this study.

Strain	Description	Reference or Source
TIGR4	Invasive clinical isolate, capsular serotype 4, sensitive to antibiotics	(36)
TIGR4ΔspxB (SPJV29)	TIGR4 derivative with insertionally inactivated spxB::ermB, erythromycin resistance, hydrogen peroxide deficient strain	(37)
TIGR4ΔlctO (SPJV42)	TIGR4 derivative with insertionally inactivated lctO::aad9, spectinomycin resistance, hydrogen peroxide deficient strain	(9)
TIGR4ΔspxBΔlctO (SPJV41)	TIGR4 derivative with spxB and lctO gene deletion by insertion-deletion with erythromycin and spectinomycin cassette, respectively, hydrogen peroxide deficient strain	(9)
EF3030	Invasive clinical isolate, capsular serotype 19F, sensitive to antibiotics	(69)
EF3030ΔspxBΔlctO (SPJV49)	EF3030 derivative with spxB and lctO gene deletion by insertion-deletion with erythromycin and spectinomycin cassette, respectively, hydrogen peroxide deficient strain	(37)
R6	Laboratory unencapsulated isolate, derivative of D39, serotype 2	(35)

1225

Figure 1

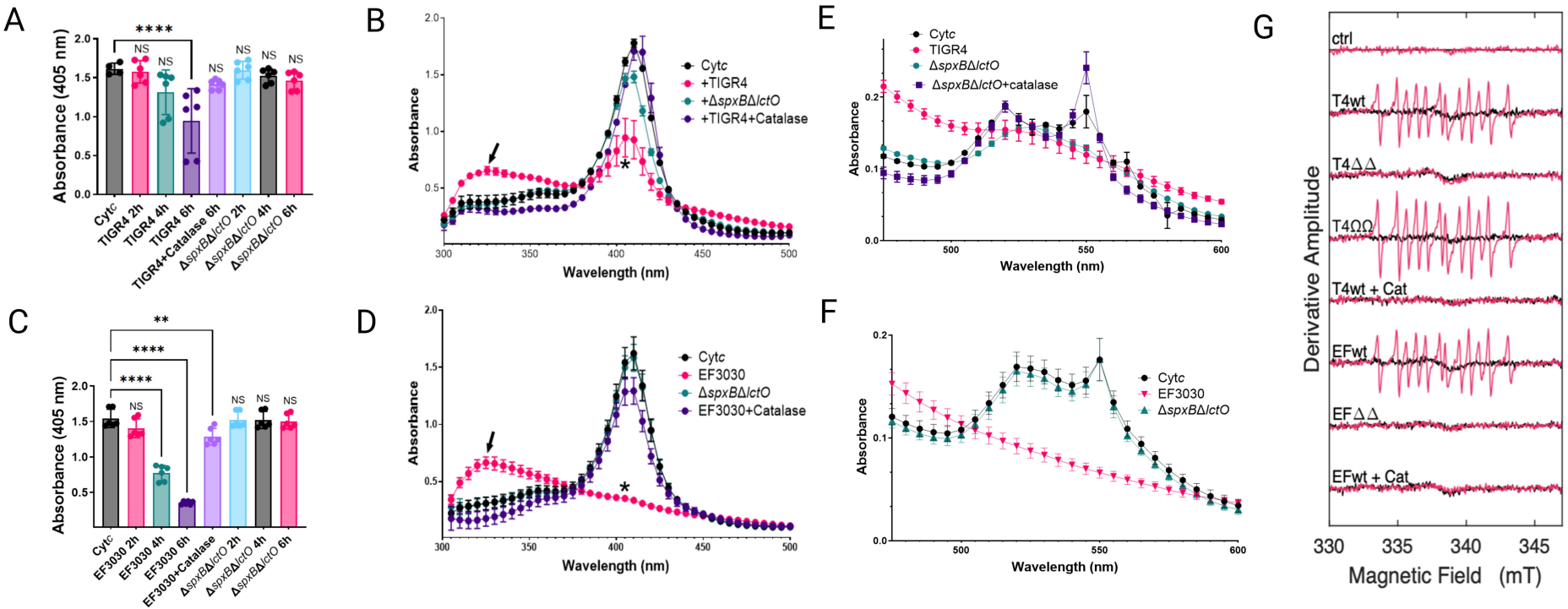
A
Absorbance (405 nm)
****
NS
Cytc
TIGR4 2h
TIGR4 4h
TIGR4 6h
TIGR4+Catalase 6h
ΔspxBΔlctO 2h
ΔspxBΔlctO 4h
ΔspxBΔlctO 6h
B
Absorbance
Wavelength (nm)
Cytc
+TIGR4
+ΔspxBΔlctO
+TIGR4+Catalase
C
Absorbance (405 nm)
**
****
EF3030 2h
EF3030 4h
EF3030 6h
EF3030+Catalase
D
Absorbance
Wavelength (nm)
Cytc
EF3030
ΔspxBΔlctO
EF3030+Catalase
E
Absorbance
Wavelength (nm)
Cytc
TIGR4
ΔspxBΔlctO
ΔspxBΔlctO+catalase
F
Absorbance
Wavelength (nm)
Cytc
EF3030
ΔspxBΔlctO
G
Derivative Amplitude
ctrl
T4wt
T4ΔΔ
T4ΩΩ
T4wt + Cat
EFwt
EFΔΔ
EFwt + Cat
Magnetic Field (mT)

Figure 2

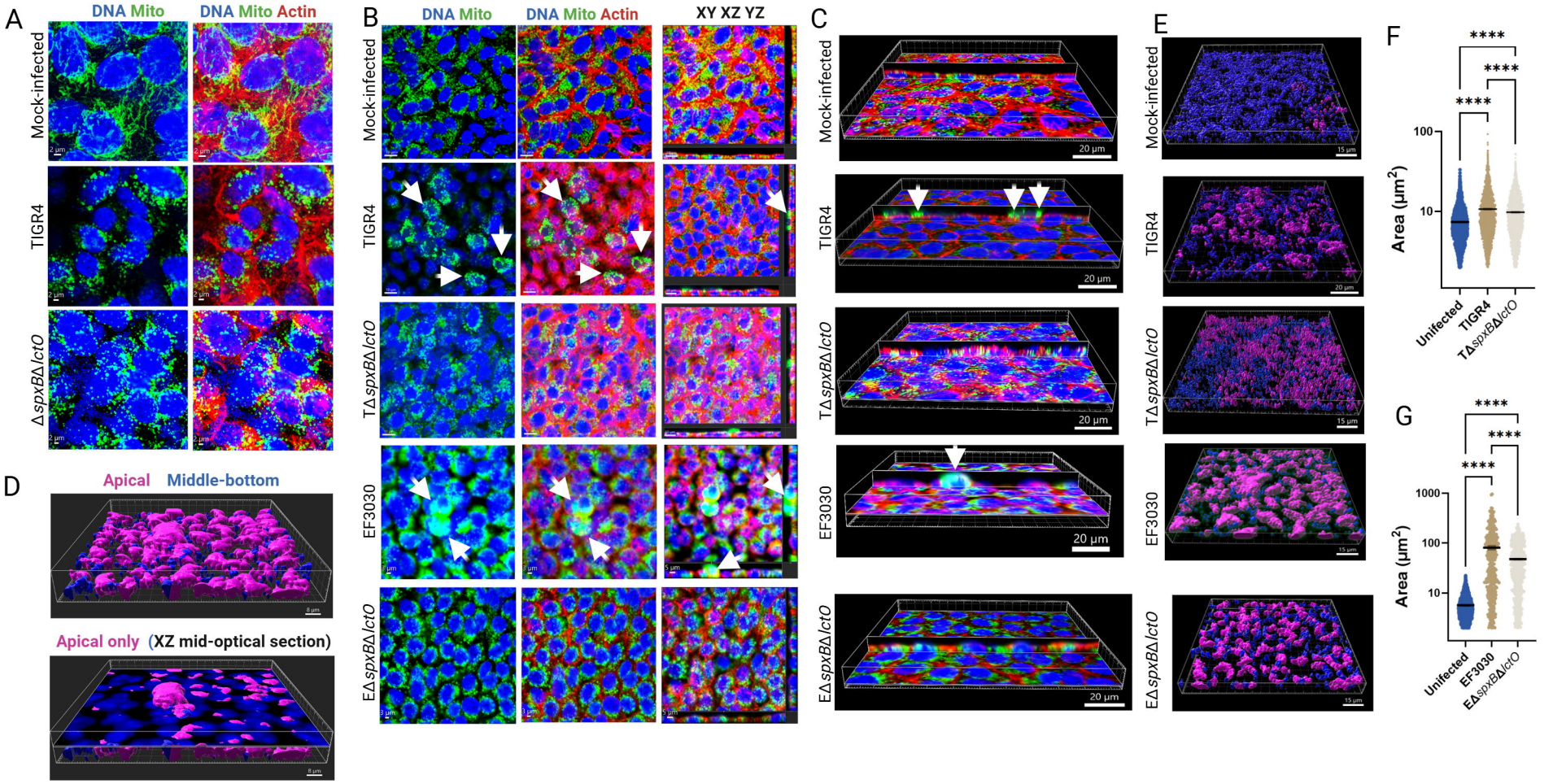
A
DNA Mito
DNA Mito Actin
Mock-infected
TIGR4
ΔspxBΔlctO
B
DNA Mito
DNA Mito Actin
XY XZ YZ
Mock-infected
TIGR4
TΔspxBΔlctO
EF3030
EΔspxBΔlctO
C
Mock-infected
TIGR4
TΔspxBΔlctO
EF3030
EΔspxBΔlctO
20 µm
D
Apical
Middle-bottom
Apical only
(XZ mid-optical section)
E
Mock-infected
TIGR4
TΔspxBΔlctO
EF3030
EΔspxBΔlctO
F
Area (µm²)
Unifected
TIGR4
TΔspxBΔlctO
G
Area (µm²)
Unifected
EF3030
EΔspxBΔlctO

Figure 3

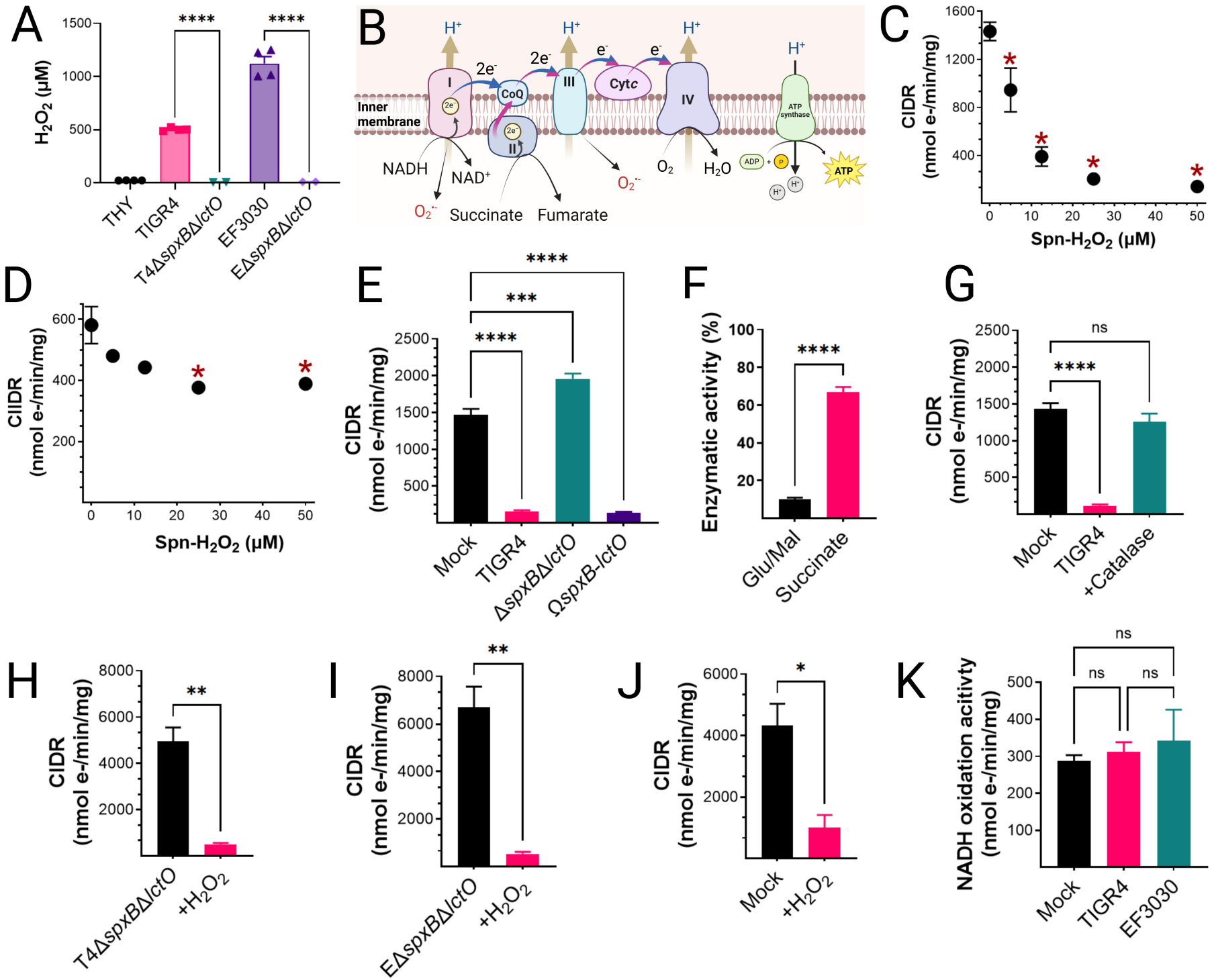
A
H_2O_2 (μM)
1500
1000
500
0
****
****
THY
TIGR4
T4ΔspxBΔlctO
EF3030
EΔspxBΔlctO
B
H+
2e-
CoQ
I
II
III
Cytc
IV
e-
Inner membrane
NADH
NAD+
Succinate
Fumarate
O2
H2O
ATP synthase
ADP
P
ATP
C
CIDR (nmol e-/min/mg)
1600
1200
800
400
Spn-H2O2 (μM)
D
CIIDR (nmol e-/min/mg)
600
400
200
Spn-H2O2 (μM)
E
CIDR (nmol e-/min/mg)
2500
2000
1500
1000
500
****
***
****
Mock
TIGR4
ΔspxBΔlctO
ΩspxB-lctO
F
Enzymatic activity (%)
100
80
60
40
20
****
Glu/Mal
Succinate
G
CIDR (nmol e-/min/mg)
2500
2000
1500
1000
500
ns
****
Mock
TIGR4
+Catalase
H
CIDR (nmol e-/min/mg)
8000
6000
4000
2000
**
T4ΔspxBΔlctO
+H2O2
I
CIDR (nmol e-/min/mg)
8000
6000
4000
2000
**
EΔspxBΔlctO
+H2O2
J
CIDR (nmol e-/min/mg)
6000
4000
2000
*
Mock
+H2O2
K
NADH oxidation acitivty (nmol e-/min/mg)
500
400
300
200
100
ns
ns
ns
Mock
TIGR4
EF3030

Figure 4

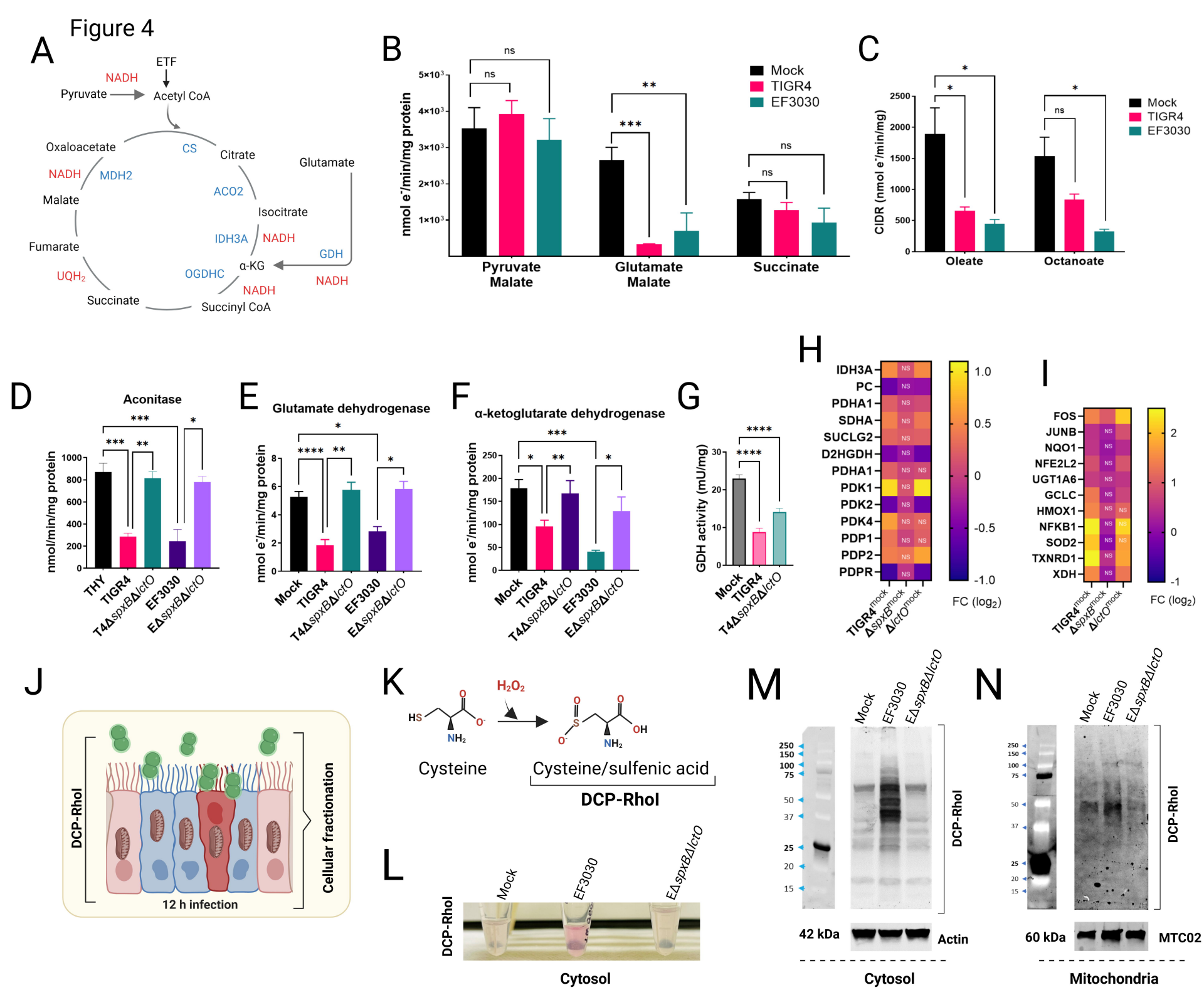
A
ETF
NADH
Pyruvate
Acetyl CoA
Oxaloacetate
CS
Citrate
Glutamate
NADH
MDH2
ACO2
Malate
Isocitrate
IDH3A
NADH
Fumarate
GDH
α-KG
UQH2
OGDHC
NADH
NADH
Succinate
Succinyl CoA
B
nmol e⁻/min/mg protein
Mock
TIGR4
EF3030
Pyruvate Malate
Glutamate Malate
Succinate
C
CIDR (nmol e⁻/min/mg)
Oleate
Octanoate
D
Aconitase
nmol/min/mg protein
THY
TIGR4
T4ΔspxBΔlctO
EF3030
EΔspxBΔlctO
E
Glutamate dehydrogenase
F
α-ketoglutarate dehydrogenase
G
GDH activity (mU/mg)
H
IDH3A
PC
PDHA1
SDHA
SUCLG2
D2HGDH
PDHA1
PDK1
PDK2
PDK4
PDP1
PDP2
PDPR
FC (log2)
I
FOS
JUNB
NQO1
NFE2L2
UGT1A6
GCLC
HMOX1
NFKB1
SOD2
TXNRD1
XDH
J
DCP-Rhol
12 h infection
Cellular fractionation
K
H2O2
Cysteine
Cysteine/sulfenic acid
DCP-Rhol
L
Mock
EF3030
EΔspxBΔlctO
DCP-Rhol
Cytosol
M
Mock
EF3030
EΔspxBΔlctO
DCP-Rhol
42 kDa
Actin
Cytosol
N
Mock
EF3030
EΔspxBΔlctO
DCP-Rhol
60 kDa
MTC02
Mitochondria

Figure 5

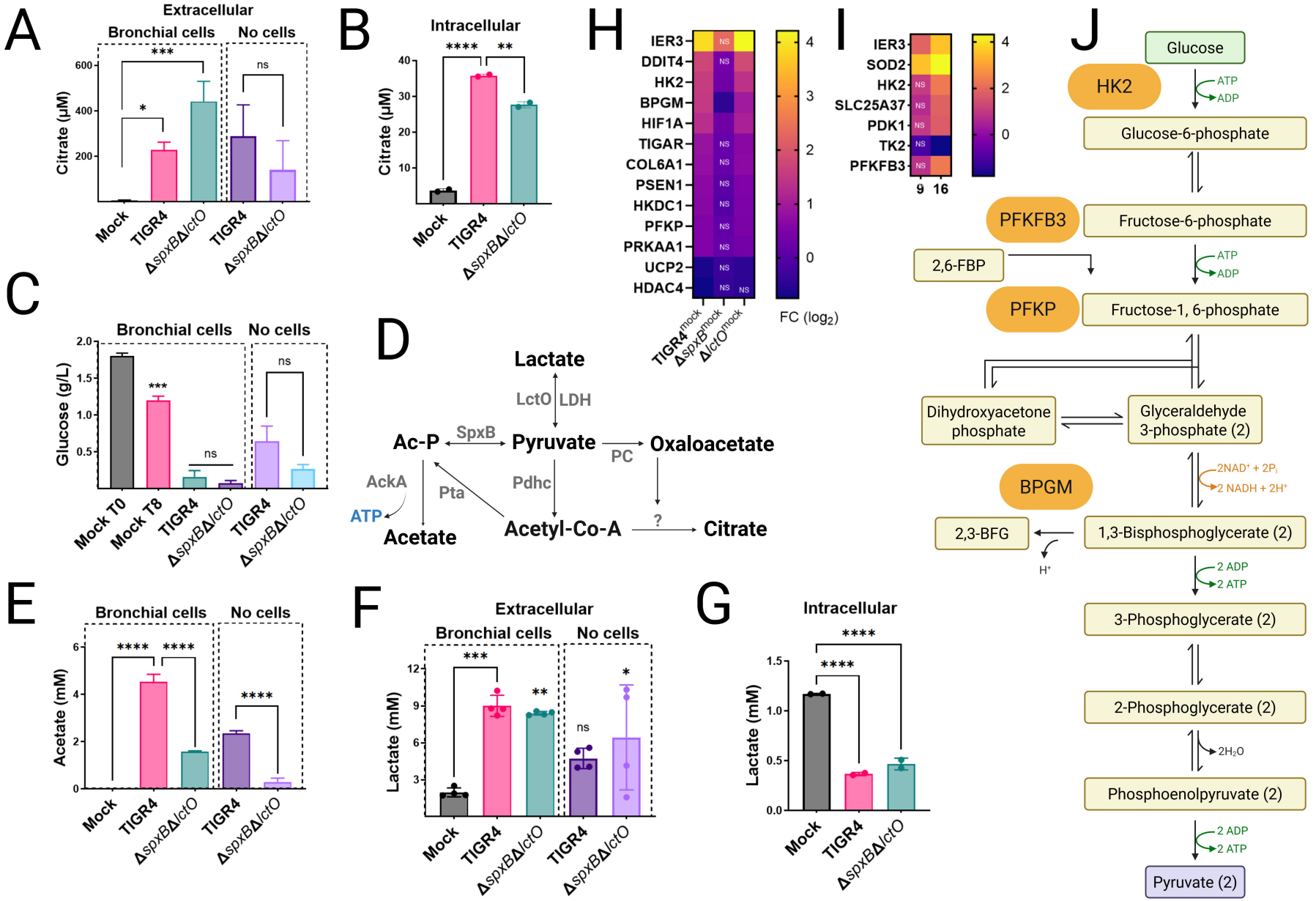
A
Extracellular
Bronchial cells
No cells
Citrate (µM)
Mock
TIGR4
ΔspxBΔlctO
B
Intracellular
Citrate (µM)
C
Bronchial cells
No cells
Glucose (g/L)
Mock T0
Mock T8
D
Lactate
LctO
LDH
Ac-P
SpxB
Pyruvate
PC
Oxaloacetate
AckA
ATP
Pta
Pdhc
Acetate
Acetyl-Co-A
?
Citrate
E
Acetate (mM)
F
Lactate (mM)
G
Intracellular
H
IER3
DDIT4
HK2
BPGM
HIF1A
TIGAR
COL6A1
PSEN1
HKDC1
PFKP
PRKAA1
UCP2
HDAC4
FC (log2)
I
SOD2
SLC25A37
PDK1
TK2
PFKFB3
J
Glucose
HK2
ATP
ADP
Glucose-6-phosphate
PFKFB3
Fructose-6-phosphate
2,6-FBP
PFKP
Fructose-1, 6-phosphate
Dihydroxyacetone phosphate
Glyceraldehyde 3-phosphate (2)
BPGM
2,3-BFG
1,3-Bisphosphoglycerate (2)
2 ADP
2 ATP
3-Phosphoglycerate (2)
2-Phosphoglycerate (2)
Phosphoenolpyruvate (2)
Pyruvate (2)

Figure 6

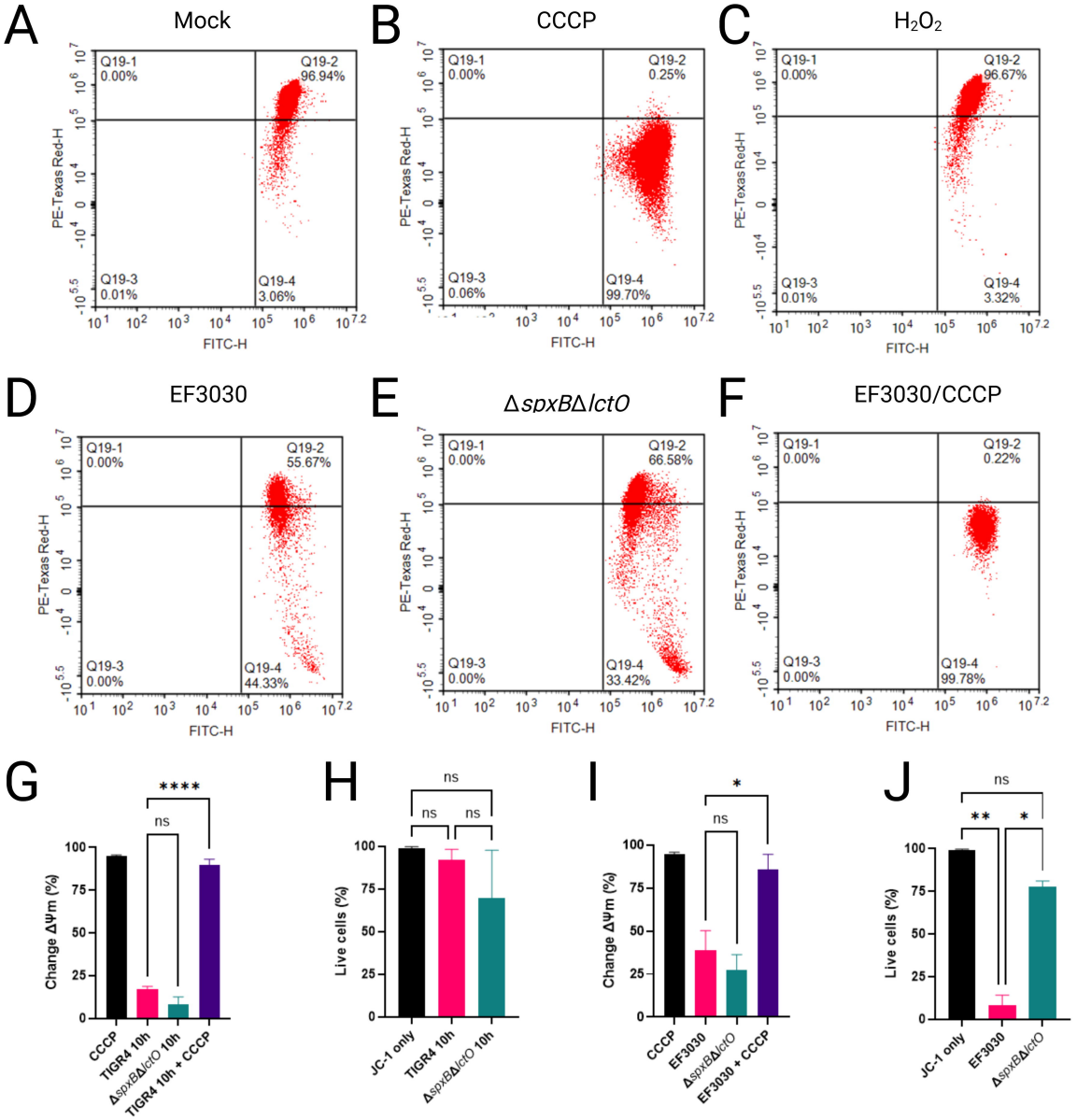
A
Mock
Q19-1 0.00%
Q19-2 96.94%
Q19-3 0.01%
Q19-4 3.06%
B
CCCP
Q19-1 0.00%
Q19-2 0.25%
Q19-3 0.06%
Q19-4 99.70%
C
H2O2
Q19-1 0.00%
Q19-2 96.67%
Q19-3 0.01%
Q19-4 3.32%
D
EF3030
Q19-1 0.00%
Q19-2 55.67%
Q19-3 0.00%
Q19-4 44.33%
E
ΔspxBΔlctO
Q19-1 0.00%
Q19-2 66.58%
Q19-3 0.00%
Q19-4 33.42%
F
EF3030/CCCP
Q19-1 0.00%
Q19-2 0.22%
Q19-3 0.00%
Q19-4 99.78%
PE-Texas Red-H
FITC-H
G
Change ΔΨm (%)
CCCP
TIGR4 10h
ΔspxBΔlctO 10h
TIGR4 10h + CCCP
****
ns
H
Live cells (%)
JC-1 only
TIGR4 10h
ΔspxBΔlctO 10h
ns
ns
ns
I
Change ΔΨm (%)
CCCP
EF3030
ΔspxBΔlctO
EF3030 + CCCP
*
ns
J
Live cells (%)
JC-1 only
EF3030
ΔspxBΔlctO
ns
**
*

Figure 7

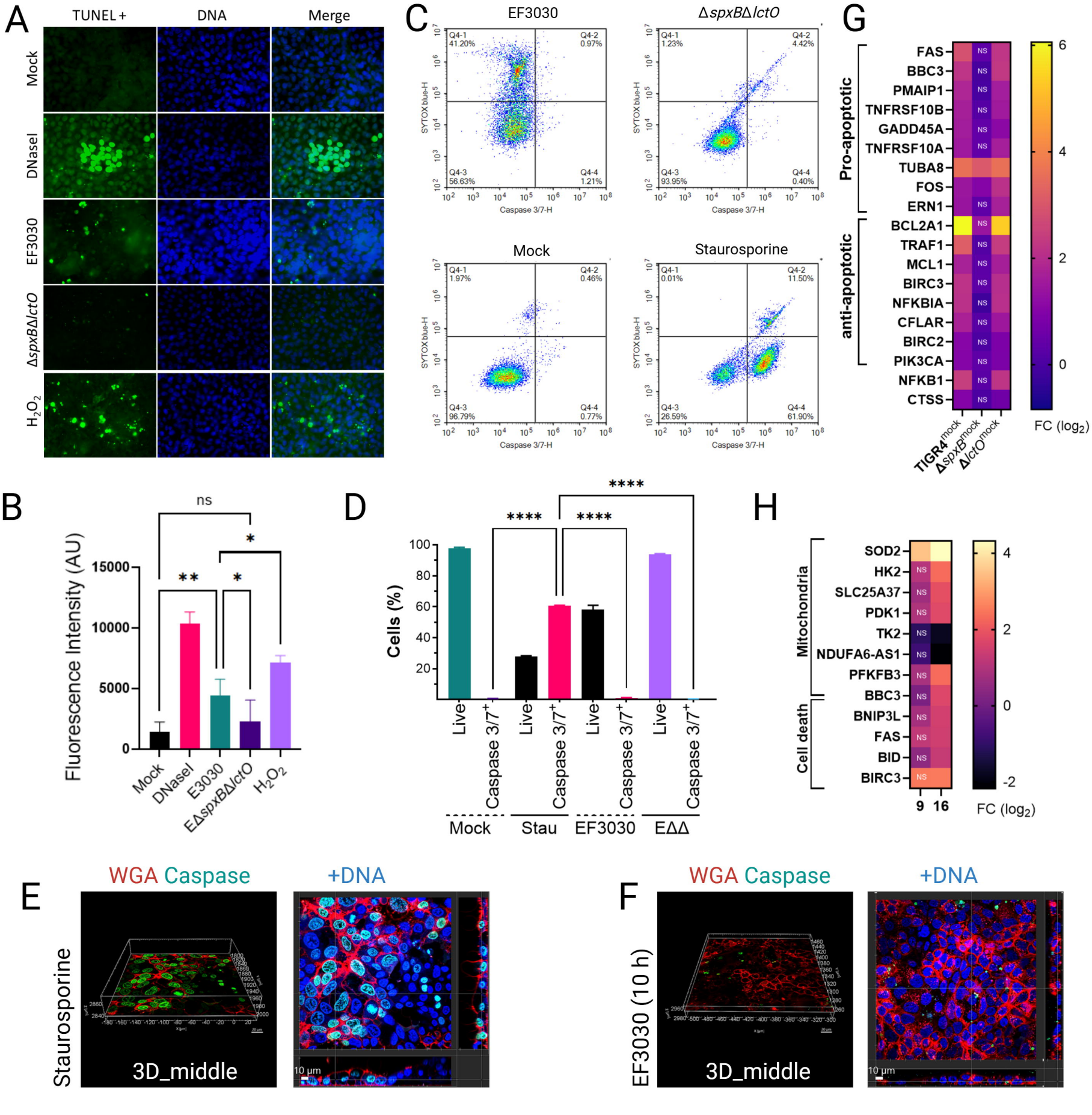
A
TUNEL +
DNA
Merge
Mock
DNaseI
EF3030
ΔspxBΔlctO
H2O2
C
EF3030
ΔspxBΔlctO
Mock
Staurosporine
Q4-1 41.20%
Q4-2 0.97%
Q4-3 56.63%
Q4-4 1.21%
Q4-1 1.23%
Q4-2 4.42%
Q4-3 93.95%
Q4-4 0.40%
Q4-1 1.97%
Q4-2 0.46%
Q4-3 96.79%
Q4-4 0.77%
Q4-1 0.01%
Q4-2 11.50%
Q4-3 26.59%
Q4-4 61.90%
SYTOX blue-H
Caspase 3/7-H
G
Pro-apoptotic
anti-apoptotic
FAS
BBC3
PMAIP1
TNFRSF10B
GADD45A
TNFRSF10A
TUBA8
FOS
ERN1
BCL2A1
TRAF1
MCL1
BIRC3
NFKBIA
CFLAR
BIRC2
PIK3CA
NFKB1
CTSS
NS
TIGR4mock
ΔspxBmock
ΔlctOmock
FC (log2)
B
ns
*
**
*
Fluorescence Intensity (AU)
15000
10000
5000
0
Mock
DNaseI
E3030
EΔspxBΔlctO
H2O2
D
****
****
****
Cells (%)
100
80
60
40
20
Live
Caspase 3/7+
Mock
Stau
EF3030
EΔΔ
H
Mitochondria
Cell death
SOD2
HK2
SLC25A37
PDK1
TK2
NDUFA6-AS1
PFKFB3
BBC3
BNIP3L
FAS
BID
BIRC3
NS
9
16
FC (log2)
E
WGA Caspase
+DNA
Staurosporine
3D_middle
10 µm
F
WGA Caspase
+DNA
EF3030 (10 h)
3D_middle
10 µm